UNIVERSITY OF MINNESOTA
ST. ANTHONY FALLS HYDRAULIC LABORATORY

Project Report No. 292

DATA ANALYSIS AND NUMERICAL MODELING OF FLOW IN THE 1:14 SCALE LCC MODEL

by

Charles C. S. Song, Mingshun Yuan
Qun Wang, and Jianming He

Prepared for

DAVID TAYLOR SHIPS RESEARCH AND DEVELOPMENT CENTER
U. S. Navy

Contract No. N6153388 M0602

June 1989
Minneapolis, Minnesota

TABLE OF CONTENTS

LIST OF FIGURES

Figure No.

I. INTRODUCTION

A 1:14 scale model of the Large Cavitation Channel (LCC) was built and tested by Voith Hydro, Inc. [1]. The velocity profiles on the central plane of symmetry was surveyed using Pitot tubes at stations P1 to P7 as shown in Fig. 1. Later, additional measurements were made with LVD at stations L1 to L4 [2]. These measurements indicated the existence of unusually thick boundary layers on the top wall at the test section and poor flow quality in the diffuser when the honeycomb for turbulence management was present. Some improvements on mean velocity profiles were found possible by either completely or partially removing the honeycomb.

The flow characteristics as indicated by the limited amount of data are extremely difficult to understand. It also appears too costly and impractical to take sufficient amounts of additional data to completely map and understand the flow field in the model channel. Even if sufficient amounts of data could be obtained, it would still be virtually impossible to predict the prototype flow characteristics because of the scale effect.

Mathematical modeling work carried out during the design stage of the LCC project was extended for the purpose of interpreting the meaning of the limited amount of apparently abnormal data and also to help predict the prototype flow condition. During the design stage, only two–dimensional nonviscous flow models of the contraction and turning vanes were used to help determine the shapes of the contraction and the turning vanes. However, the data taken at the 1:14 model clearly indicates the need for a three–dimensional nonviscous flow model of the contraction and, at least, a two–dimensional turbulent flow model of the diffuser. Recent experience on diffuser design for the HYKAT water tunnel [3] indicates that the diffuser flow is very unstable and sensitive to the inflow velocity distribution and Reynold number.

The two–dimensional and a three–dimensional Euler equation model for the contraction and a two–dimensional turbulent flow model of the test section–diffuser region were used to study the flow characteristics in the upper leg of the LCC model and the prototype. By comparing the data taken from the 1:14 scale model with the computational results, it is hoped to elucidate the complex flow behavior of the LCC. This report summaries the results of the mathematical modeling work for the purpose of elucidating the hydrodynamic characteristics of LCC.

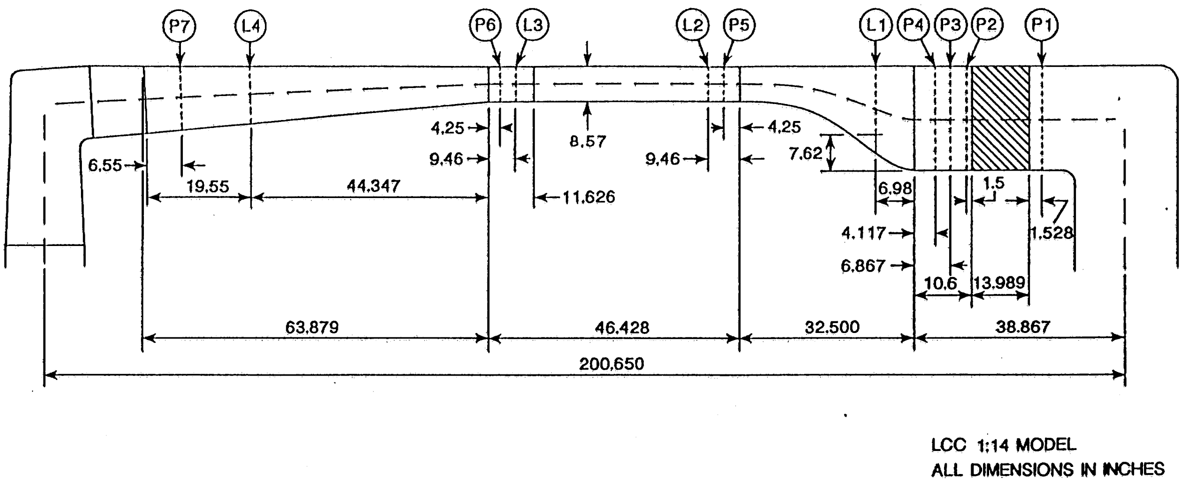

Fig. 1 Upper leg of LCC model showing location of measurements.

II. DESCRIPTION OF MATHEMATICAL MODELS

A. GOVERNING EQUATIONS OF WEAKLY COMPRESSIBLE FLOWS

The upper leg of LCC is divided into two zones for mathematical modeling purposes. These are the contraction–test section zone and the test section–diffuser zone. Since the flow in the contraction is not sensitive to viscosity, Euler equation based two- and three-dimensional models were used to calculate the flow in the contraction–test section zone. On the other hand, a two-dimensional turbulent flow model was used to simulate the flow in the test section–diffuser zone.

Recently developed governing equations for weakly compressible flows [4], as briefly described below, are used. Assuming the flow to be barotropic, the equation of continuity,

$$\frac{D\rho}{Dt} + \rho\nabla\cdot\vec{v} = 0 \tag{1}$$

is transformed into the following equation.

$$\frac{Dp}{Dt} + \rho a^2\nabla\cdot\vec{v} = 0 \tag{2}$$

Here, a is the speed of sound given by

$$a^2 = \frac{dp}{d\rho} \tag{3}$$

The weakly compressible flow is the flow with such a small Mach number that both a and ρ in Eq. (2) may be regarded as constants. It follows that the bulk modulus of elasticity $k = \rho a^2$ is also a constant for a weakly compressible flow. Since the convective terms are $0(M^2)$, they can be dropped and Eq. 2 is simplified to

$$\frac{\partial p}{\partial t} + \nabla\cdot k\vec{v} = 0 \tag{4}$$

The first term in Eq. 2 is retained for two reasons. Firstly, the term may not be small when the flow is highly unsteady. Secondly, the hyperbolic nature of the system is preserved by retaining this term.

The equation of motion for incompressible flows,

$$\frac{D\vec{v}}{Dt} + \frac{1}{\rho}\nabla p = \nu\,\nabla^2\vec{v} \tag{5}$$

is accurate to the first order of M and appropriate for the weakly compressible flow. Thus, the governing equations of the weakly compressible flows are the set Eqs. (2) and (5) or the set Eqs. (4) and (5). When the second set is used to calculate a steady flow, the converged solution is the same as that of the incompressible flow. In other words the first order effect of compressibility is tied to the flow unsteadiness.

B. EULER EQUATIONS MODEL FOR CONTRACTION

For accelerating flows in a contraction at high Reynold numbers, the viscous effect is negligible and the equation of motion reduces to

$$\frac{D\vec{v}}{Dt} + \frac{1}{\rho} \nabla p = 0 \tag{6}$$

The set, Eqs. (4) and (6), are solved numerically using MacCormack's predictor–corrector method [5].

As part of the primary boundary conditions, the velocity distribution at the entrance and the average pressure over the exit cross section are specified. The full slip condition is applied on the solid walls. In addition, the numerical procedure requires secondary boundary conditions [5] which must be chosen carefully. The boundary control method proposed by Song and Yuan [4] can accelerate the convergence rate by at least a factor of ten.

C. TURBULENT FLOW MODEL

The effect of viscosity (for a laminar flow) and turbulence are extremely important to the decelerating flow in the diffuser. The flow in the test section–diffuser part of the tunnel is undoubtedly in the turbulent regime. For this reason, a cell averaged large eddy simulation model [6] is used. The cell averaged equation of motion is

$$\frac{D\vec{v}}{Dt} + \frac{1}{\rho} \nabla p = \nu^2 \nabla \vec{v} - \overline{u_i' u_j'} \tag{7}$$

where u_i' is the subgrid scale turbulence and bar represents average over a finite volume. Smagorinsky's [7] subgrid scale turbulence model is used to model the last term of Eq. (7). This model is

$$\overline{u_i' u_j'} = \nu_T \overline{\frac{\partial u_i}{\partial x_j}} \tag{8}$$

where ν_T is the SGS diffusivity, being modeled by

$$\nu_T = (C\Delta)^2 (2\overline{S}_{ij}\overline{S}_{ij})^{1/2} \tag{9}$$

where $S_{ij} = \frac{1}{2} \left(\frac{\partial u_i}{\partial x_j} + \frac{\partial u_j}{\partial x_i} \right)$ (10)

In the above equations, C is a calibration constant and Δ represents the grid size.

With the viscous and the SGS turbulence terms, the turbulent flow model is supposed to be capable of modeling the flow near the walls by imposing the no-slip boundary condition. In practice, however, it is too costly to achieve the complete resolution of the thin wall region of the turbulent flow. For this reason, a wall function approach [8] is used to account for the effect of large velocity gradients within the wall cell on the overall flow field. In this particular case the logarithmic law is assumed to exist in the wall region and the boundary condition similar to that used by Ferziger [8] and discussed by Roggallo and Moin [9] is used.

Although the large eddy simulation approach is theoretically applicable only to three-dimensional turbulent flows, Eqs. 7 ~ 10 need not be restricted to three-dimensional flows. It will be shown later that a modified two-dimensional flow model can adequately simulate the flow on the vertical plane of symmetry where the great majority of data were taken.

Because the flow in a diffuser is very sensitive to the adverse pressure gradient, it is essential to account for the lateral diffusion of mass and momentum in the LCC diffuser. The modified equations of continuity and motion are as follows:

$$\frac{\partial p}{\partial t} + \nabla \cdot k\vec{v} = kS \tag{11}$$

and

$$\frac{D\vec{v}}{Dt} + \frac{1}{\rho} \nabla p = \nu \nabla^2 \vec{v} - \overline{u_i' u_j'} + \vec{v}S \tag{12}$$

where $S = S(x,y)$ is the strength of source (negative value implies sink) distribution. For the LCC diffuser of rectangular cross section, the following equation has been derived.

$$S(x,y) = -\frac{u(x,y)}{B(x)} \frac{dB(x)}{dx} \tag{13}$$

where $u(x,y)$ is the x-component of velocity and $B(x)$ is the width of the diffuser.

III. COMPARISON OF CALCULATIONS AND MEASUREMENTS

A. FLOW IN CONTRACTION–TEST SECTION

The results of a two–dimensional Euler equation model obtained under a previous contract was communicated to DTNSRDC in 1987 [10]. The measured longitudinal velocity distribution at the entrance and the pressure at the exit were taken as the boundary conditions. The computed pressure distribution at the entrance and velocity distribution at the exit were compared with the corresponding measured values. Very good agreements were obtained. In other words, the longitudinal velocity distribution on the center plane of the contraction is self consistent and predictable with the two–dimensional flow model. The cause of poor velocity distribution in the test section is the poor velocity distribution at the entrance and, hence, the solution to the problem must be found outside of the contraction–test section part.

The two–dimensional flow calculation mentioned above does not explain the apparent existence of secondary currents and transverse velocity components. Clearly a three–dimensional flow model is needed to further analyze the flow. This work, however, faces the difficulty of having insufficient data to be used as the boundary conditions of the mathematical model. As mentioned previously, measurements were made primarily for the longitudinal velocity component along a few vertical lines. Data on vertical velocity components is available only in a very small region at the entrance to the contraction. According to the limited amount of available data, it was estimated that the velocity at the entrance has approximately 10 degree yaw angle and 14.75 degree pitch angle.

As the first trial, the three–dimensional Euler equation model was set up with the inflow velocity distribution (the upstream end boundary condition) determined in the following way. The longitudinal velocity distribution on all vertical lines are assumed to be the same as that measured along the centerline. That is

$$u\ (o,y,z) = u(o,o,z) \tag{14}$$

of test No. 6418 [1]. The transverse velocity distribution is assumed to be given by

$$\frac{v(o,y,z)}{u(o,y,z)} = \tan\ 10^\circ \quad ; \quad \frac{w(o,y,z)}{u(o,y,z)} = \tan\ 14.75^\circ \tag{15}$$

The assumed (v,w) velocity field at the entrance is shown in Fig. 2. The corresponding vorticity field is shown in Fig. 3. The calculated velocity field and the corresponding vorticity field at the test section entrance are shown in Figs. 4 and 5, respectively. By comparing Figs. 2 and 4, it is

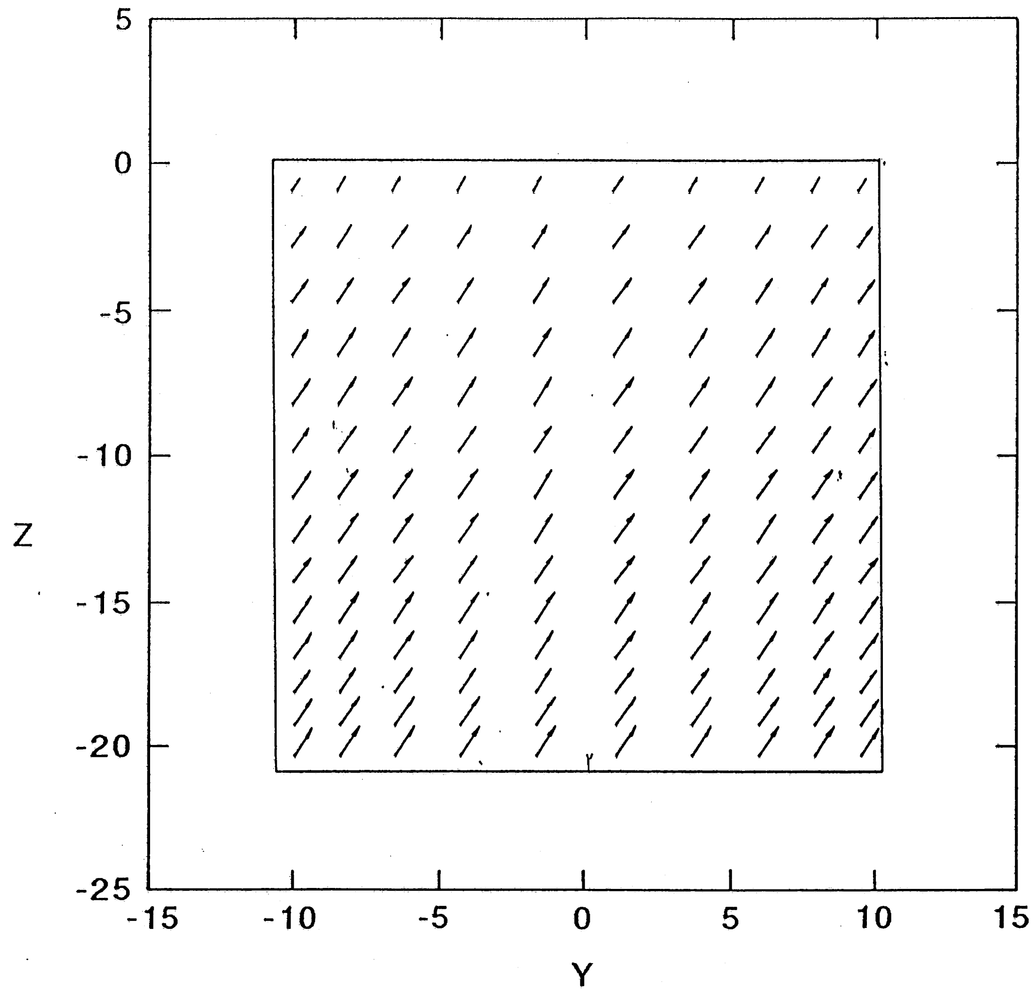

Fig. 2 Velocity vector field on entrance cross section assumed for Run No. 1 (constant direction, $v = u \tan 10^\circ$, $w = u \tan 14.75^\circ$).

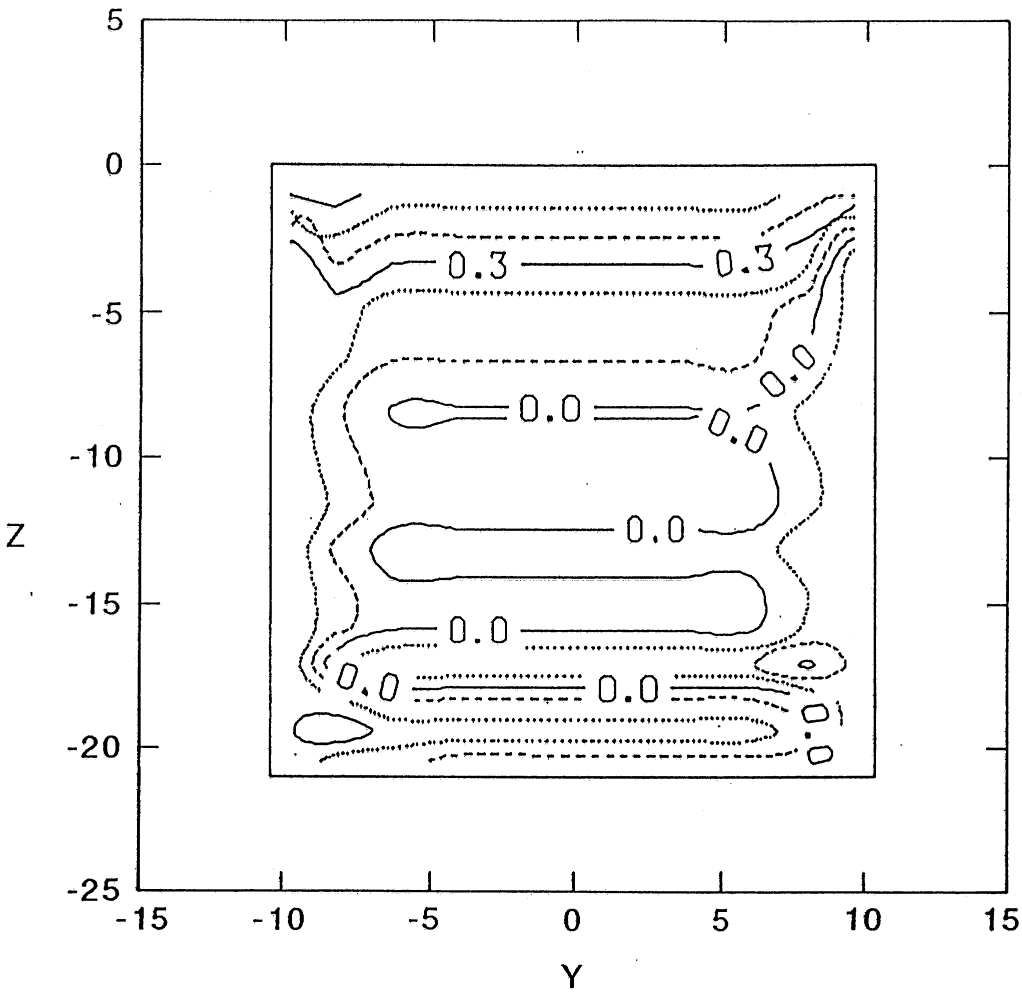

Fig. 3 Vorticity distribution at entrance cross section for Run No. 1.

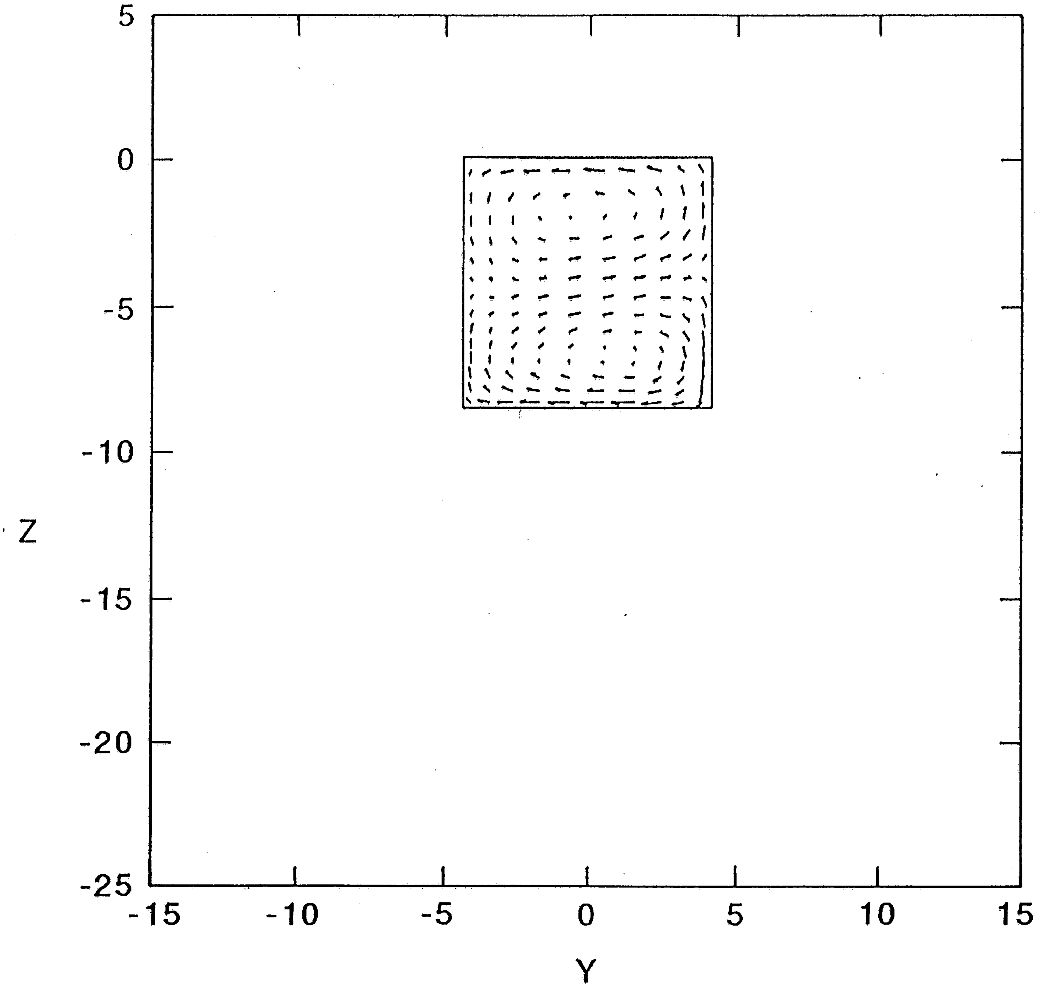

Fig. 4 Calculated velocity vector field on the test section entrance cross section, Run No. 1.

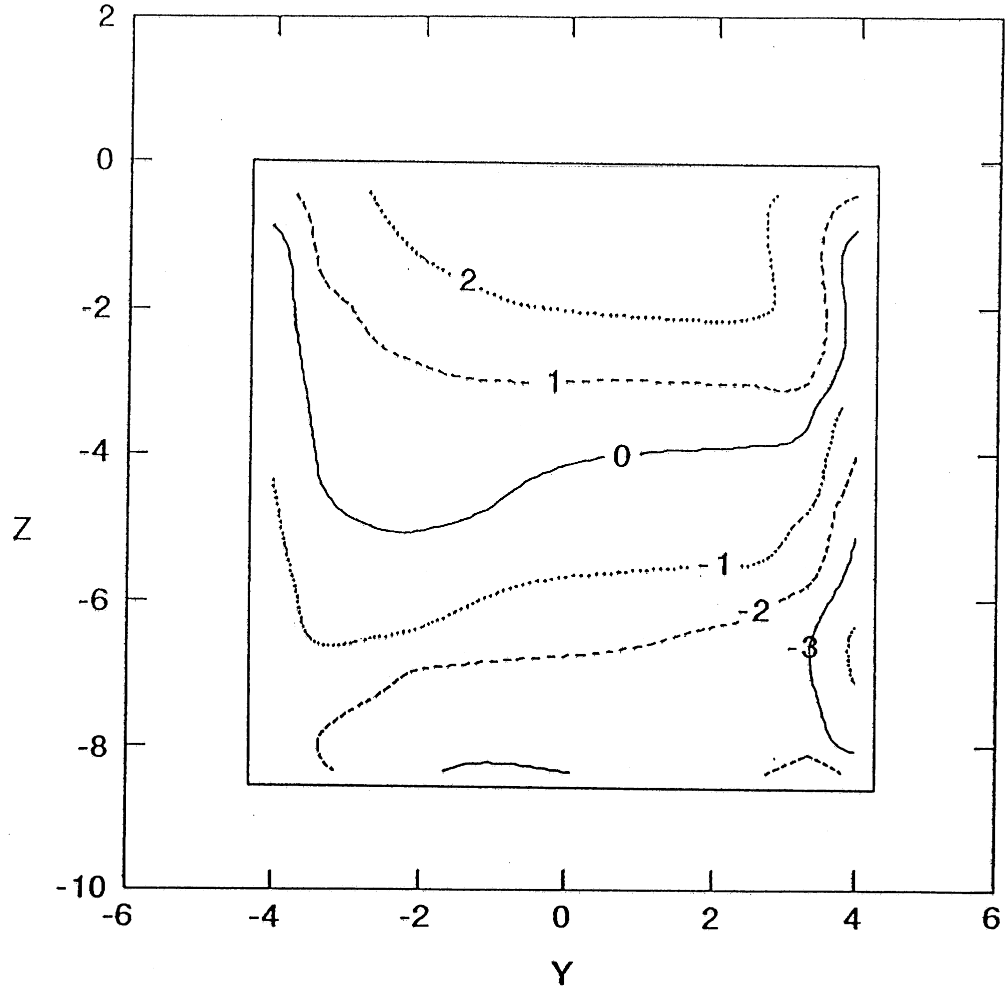

Fig. 5 Vorticity distribution on the cross section at the test section entrance, Run No. 1.

apparent that the contraction suppresses the transverse velocity field and organizes two counter rotating vortices. On the other hand, comparison of Figs. 3 and 5 reveals a different phenomenon: contraction stretches and intensifies the vorticity which enters the contraction.

The calculated and measured dimensionless lateral velocity, v/u, on the plane of symmetry at the test section entrance are shown in Fig. 6. While the mathematical model captures the general trend, it misses the asymmetry exhibited by the data.

Due to the lack of data at the contraction entrance and the uncertainties inherent in the input data, it is necessary to conduct sensitivity analysis to improve our understanding of the flow. The measured yaw and pitch angles near the center of the entrance cross section, $\alpha = 10°$ and $\beta = 14.75°$, can also be produced by a forced vortex of constant vorticity. The secondary current at the contraction entrance due to a constant vorticity of -0.7 is shown in Fig. 7. This secondary current and the longitudinal velocity distribution of Run No. 1 were used as the upstream boundary condition of Run No. 2. The resulting secondary current on the cross section at the test section entrance is shown in Fig. 8. The corresponding vorticity distribution is shown in Fig. 9. The contraction has concentrated and redistributed the vorticity. The calculated lateral velocity, v/u, on the central plane at the test section entrance is compared with the measured values in Fig. 10.

The results of the above two runs justifies the following statements:

(1) A unidirectional cross flow of nearly constant magnitude superposed on the main flow at the contraction entrance produces a pair of counter rotating vortices at the contraction exit. This vortex pair produces a symmetrical lateral velocity profile on the vertical centerline.

(2) A secondary current of constant vorticity at the contraction entrance produces single vortex at the contraction exit. This vortex produces antisymmetrical lateral velocity profiles on the centerline.

Having found the mechanisms generating symmetrical and antisymmetrical lateral velocity distributions, both of which are consistent with the available data at the contraction entrance, one can now proceed to find the combination that will give best results. Let v_1 and v_2 be the lateral velocity components and w_1 and w_2 be the corresponding vertical velocity components imposed at the inlet for Runs No. 1 and No. 2, respectively. A new run, Run No. 3, was performed on the inlet condition given by the following linear combination.

$$v_3 = 0.8\ v_1 + 0.2\ v_2 \tag{16}$$

$$w_3 = 0.8\ w_1 + 0.2\ w_2 \tag{17}$$

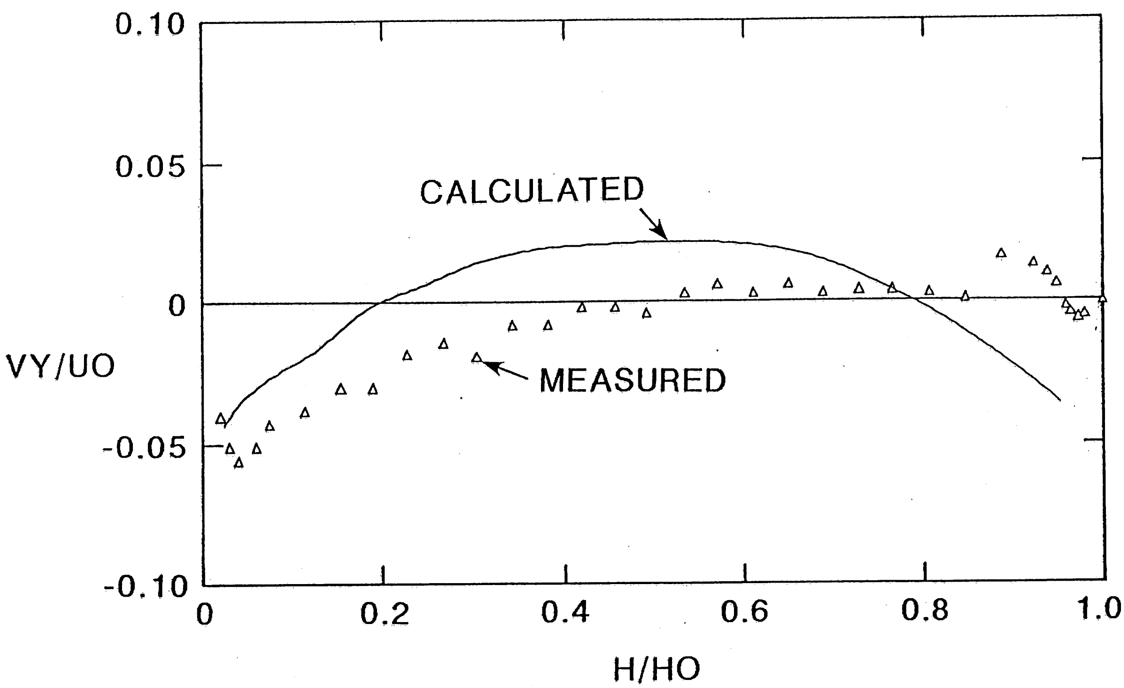

Fig. 6 Lateral velocity profile on central plane at test section entrance, comparison of computation and measurement, Run No. 1.

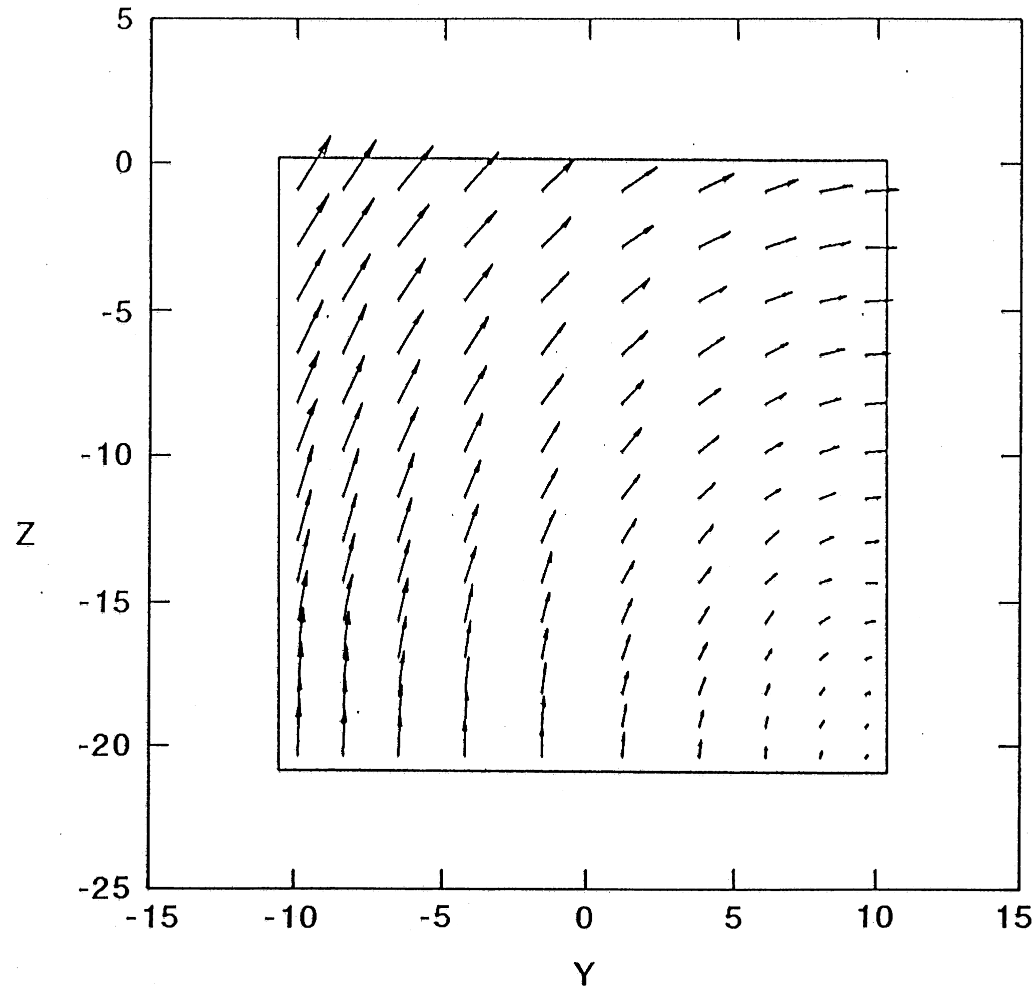

Fig. 7 Velocity field on the entrance cross section due to a constant vorticity field, U.S. boundary condition for Run No. 2.

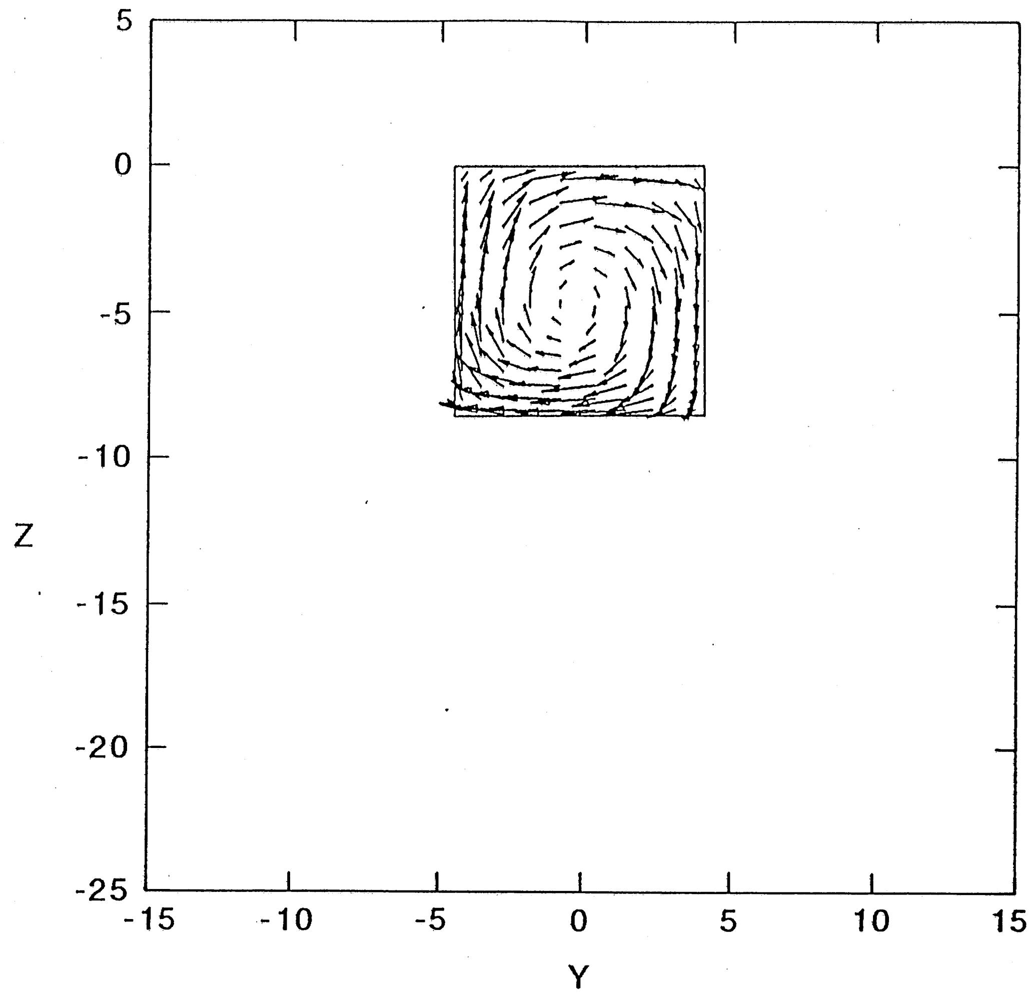

Fig. 8 Calculated velocity vector field on the test section entrance cross section, Run No. 2.

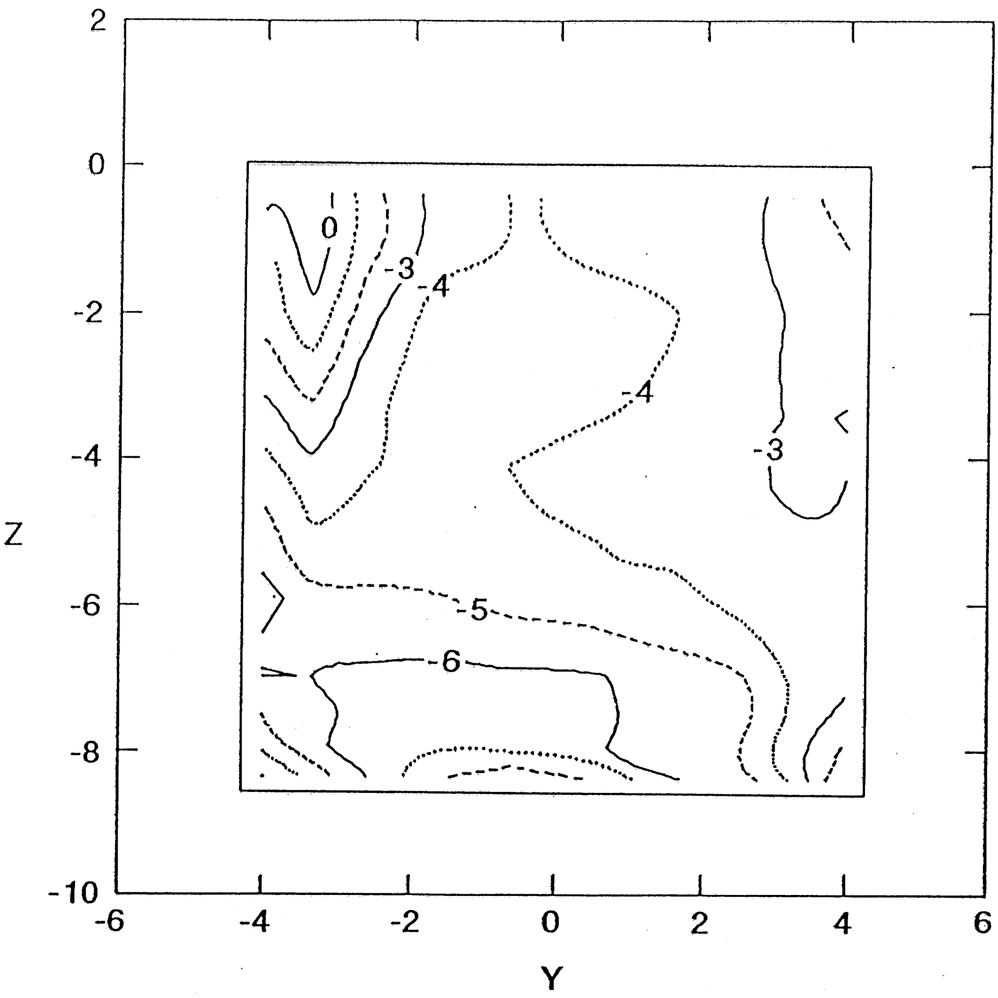

Fig. 9 Vorticity distribution on the cross section at the test section entrance, Run No. 2.

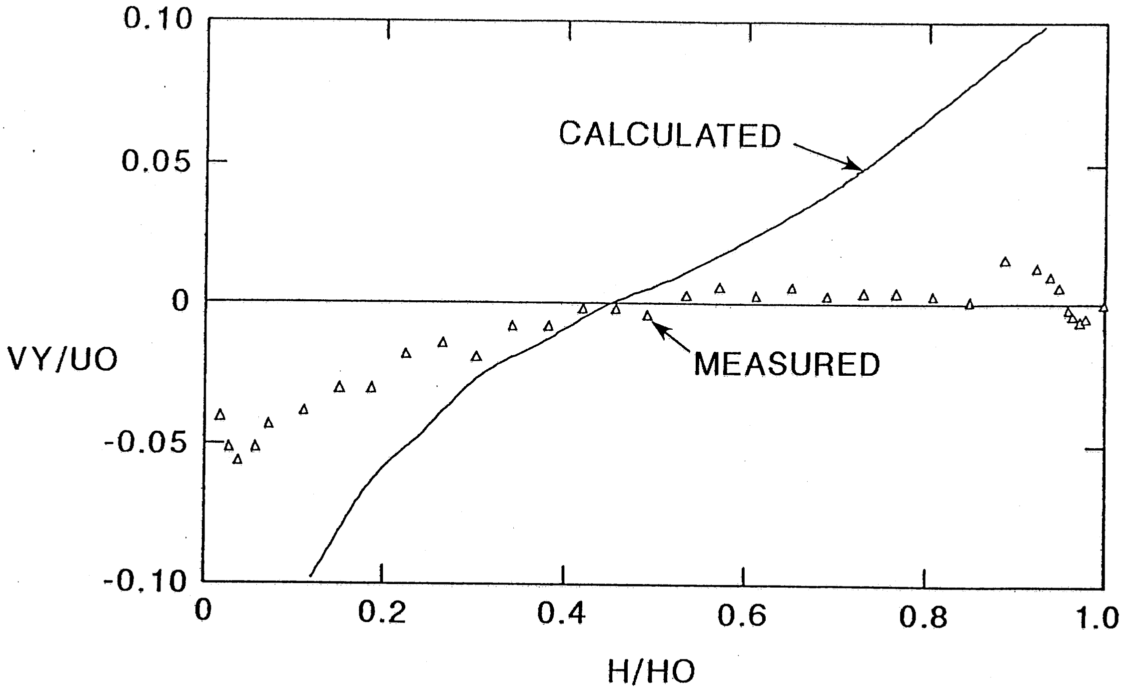

Fig. 10 Lateral velocity profile on central plane at test section entrance, comparison of computation and measurement, Run No. 2.

The imposed velocity field on the inlet cross section and the corresponding calculated velocity field on the test section inlet cross section are shown, respectively, in Figs. 11 and 12. Two counter rotating eddies of unequal sizes are observable in Fig. 12. The imposed vorticity field on the inlet cross section and the calculated vorticity field on the test section inlet are shown in Figs. 13 and 14, respectively. Figure 15 shows the comparison of calculated and measured lateral velocity distribution on the central plane at the test section entrance. Somewhat improved agreement of Run No. 3 over two previous runs indicates that a secondary current like the one shown in Fig. 12, generated by an imperfect inflow velocity profile, have existed at the test section entrance. The calculated velocity vector field on the central plane is shown in Fig. 16.

B. FLOW IN TEST SECTION–DIFFUSER

The modified two–dimensional turbulent flow model containing distributed sink as described in a previous section has been used for this portion of the study. This model needed practically no calibration work. The only coefficient that required adjustment was the coefficient for the subgrid scale turbulence model of Smagorinsky. Five case studies as described below were carried out.

Case 1. LDV measurement without honeycomb ($Re = 3.2\text{x}10^6$).

The time averaged velocity distribution measured at L2 (test section entrance) was used as the upstream boundary condition for the test section–diffuser model. A constant pressure at the downstream end was assumed. The calculated and the measured velocity profile at L3 (diffuser entrance) are shown in Fig. 17. A similar comparison of L4, a station further downstream, is shown in Fig. 18. Excluding the thin layers next to the boundaries, the agreements between calculated and measured values are quite good. A series of calculated velocity profiles for this case are plotted in Fig. 19. It is noteworthy that, at this Reynolds number and the inflow condition, there is a very small separation bubble on the upper wall at the end of the diffuser. Because all measurements were carried out upstream of the separation bubble, the flow separation could not be detected.

Calculated pressure distribution along the boundaries and the discharge ratio RQ are plotted in Fig. 20. The discharge ratio, defined as the ratio of the discharges through the upper half and the lower half of the diffuser cross section, is a parameter representing the degree of flow asymmetry. The discharge ratio is equal to the unity when the velocity profile is symmetrical. As indicated in Figure 20, if $RQ < 1$ and decreases in the downstream direction, the flow tends to be attracted to the bottom walls and a flow separation is more likely to occur on the upper wall. Experiences with the HYKAT project [3] show that the evolution of the velocity profiles in a diffuser is extremely sensitive to the boundary layer thickness at the entrance to the diffuser. When the boundary layer on the upper wall is slightly thicker than that of the bottom wall at the entrance, as in this case, the diffuser tends to shift the flow towards the bottom wall promoting flow asymmetry and separation.

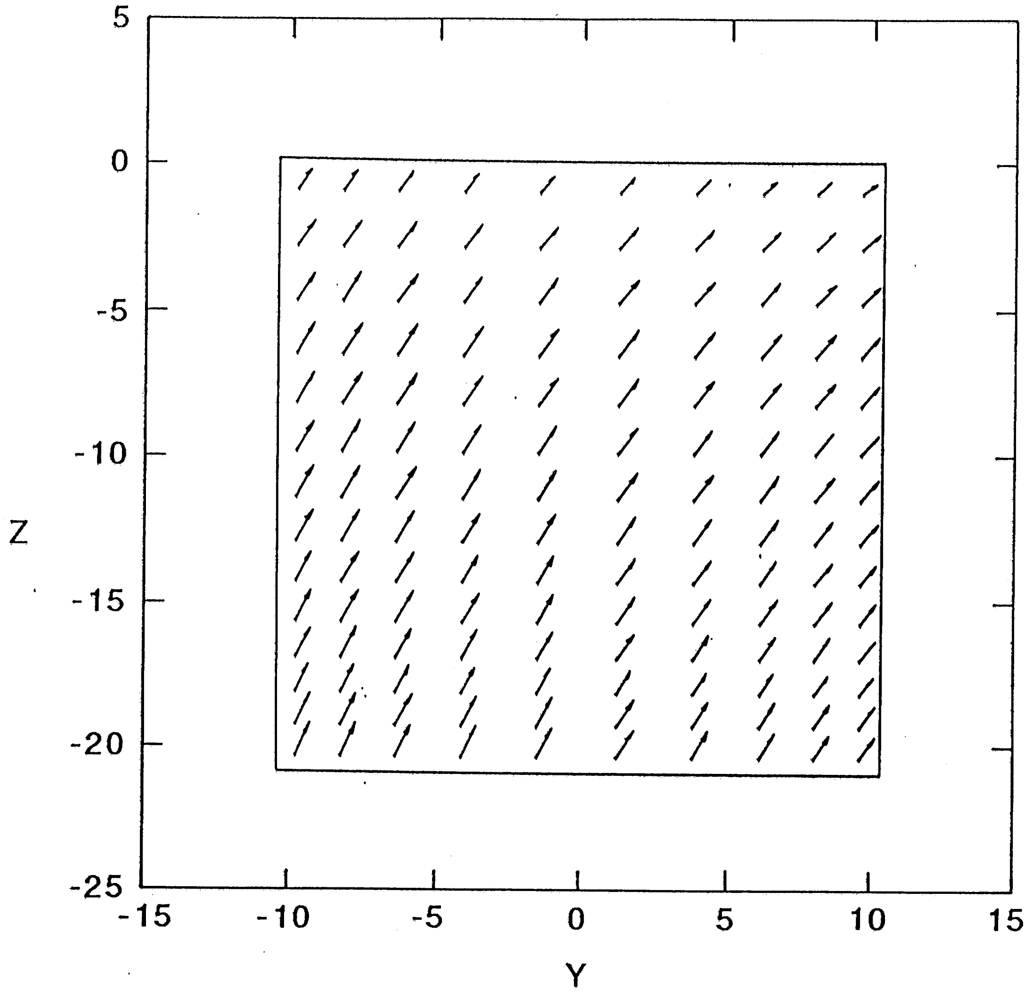

Fig. 11 Velocity vector field on entrance cross section assumed for Run No. 3.

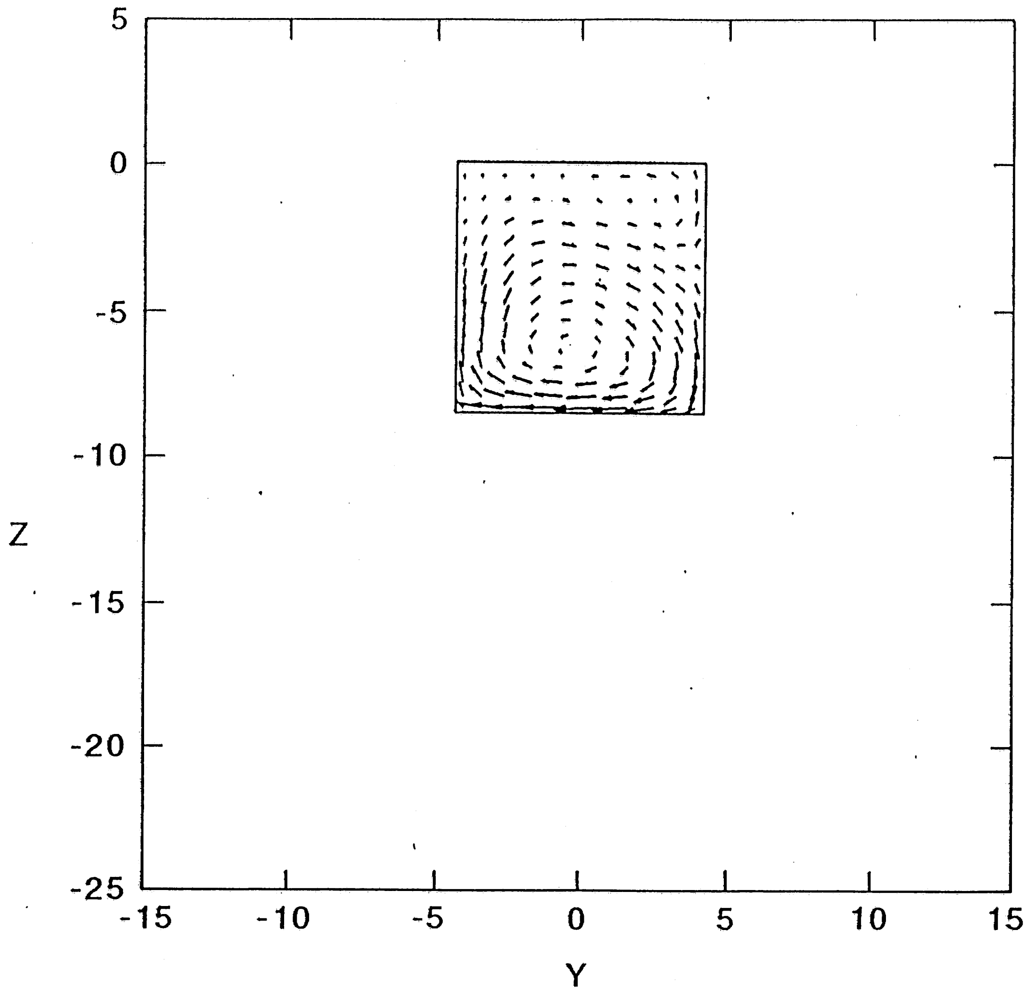

Fig. 12 Calculated velocity vector field on the last section entrance cross section, Run No. 3

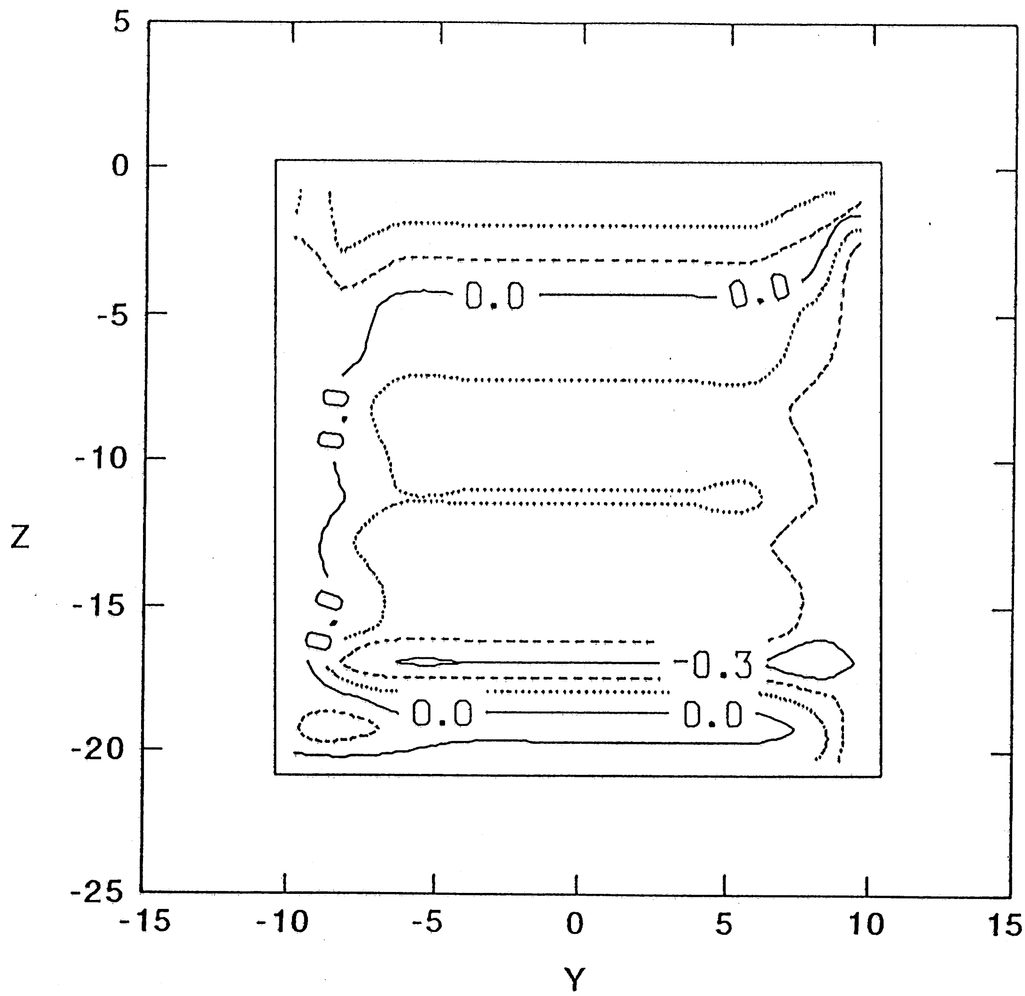

Fig. 13 Vorticity distribution at entrance cross section for Run No. 3.

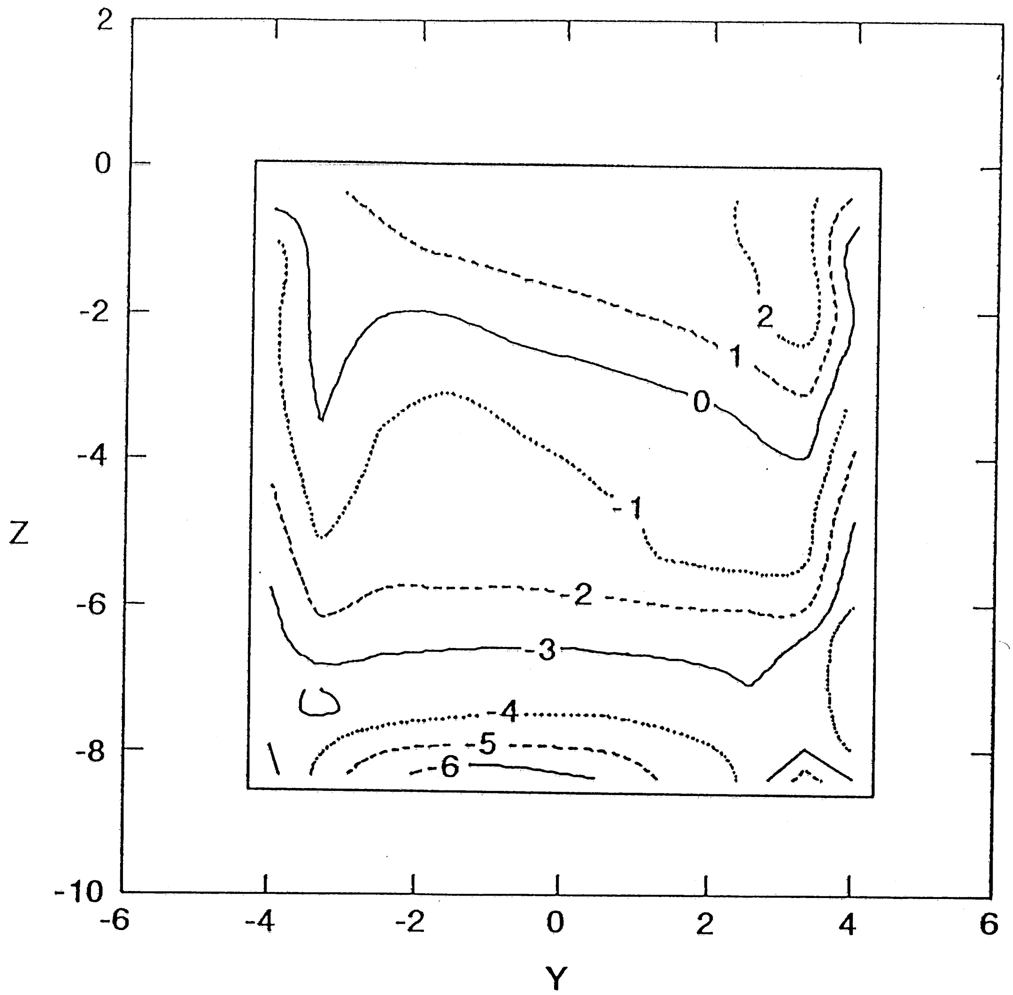

Fig. 14 Calculated vorticity field on the test section entrance cross section, Run No. 3.

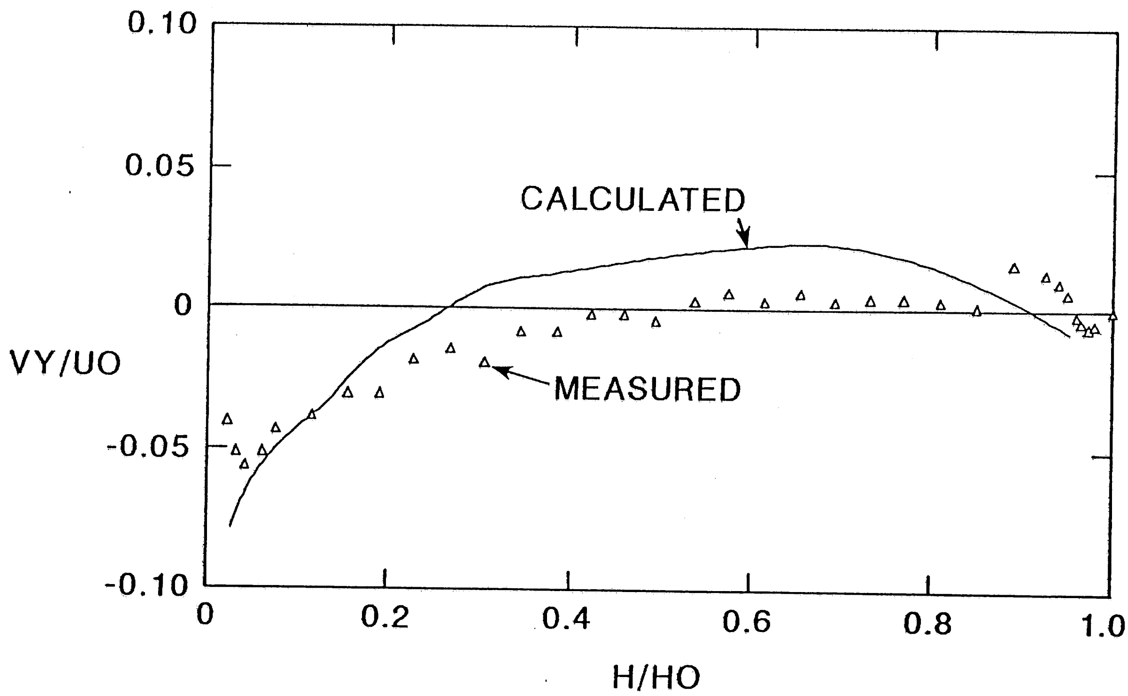

Fig. 15 Lateral velocity profile on central plane at test section entrance, comparison of computation and measurement, Run No. 3.

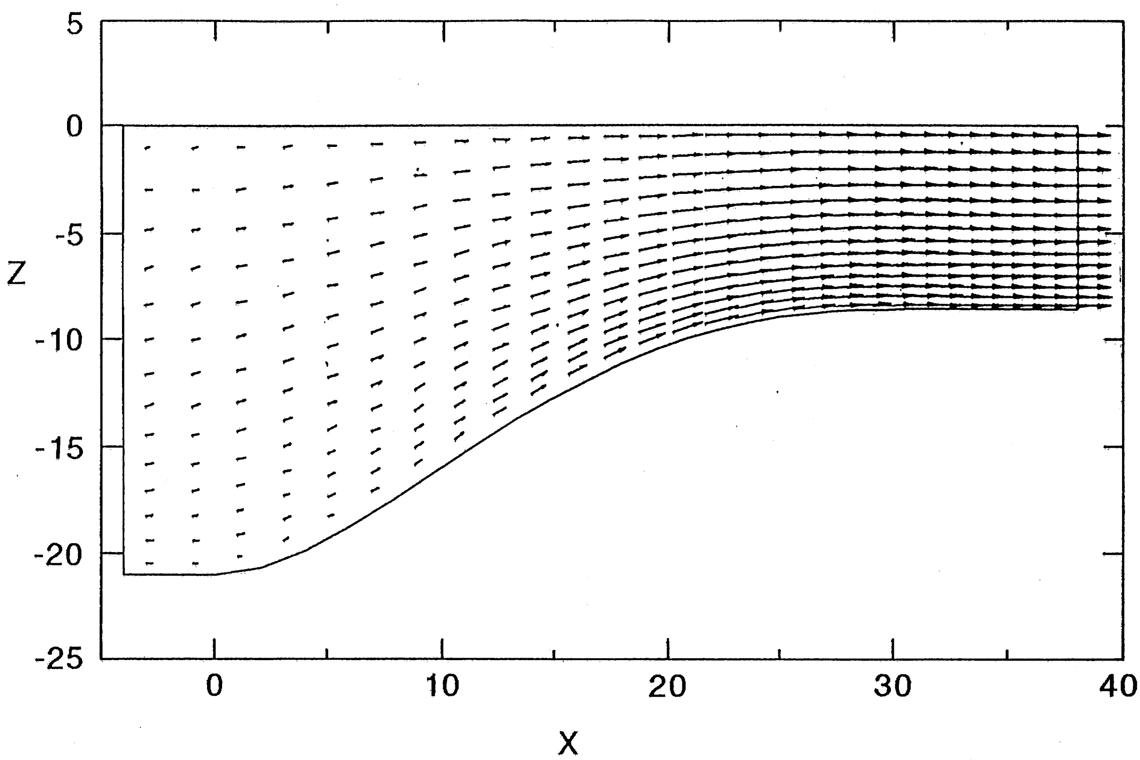

Fig. 16 Calculated velocity vector field on the center plane of symmetry, Run No. 3.

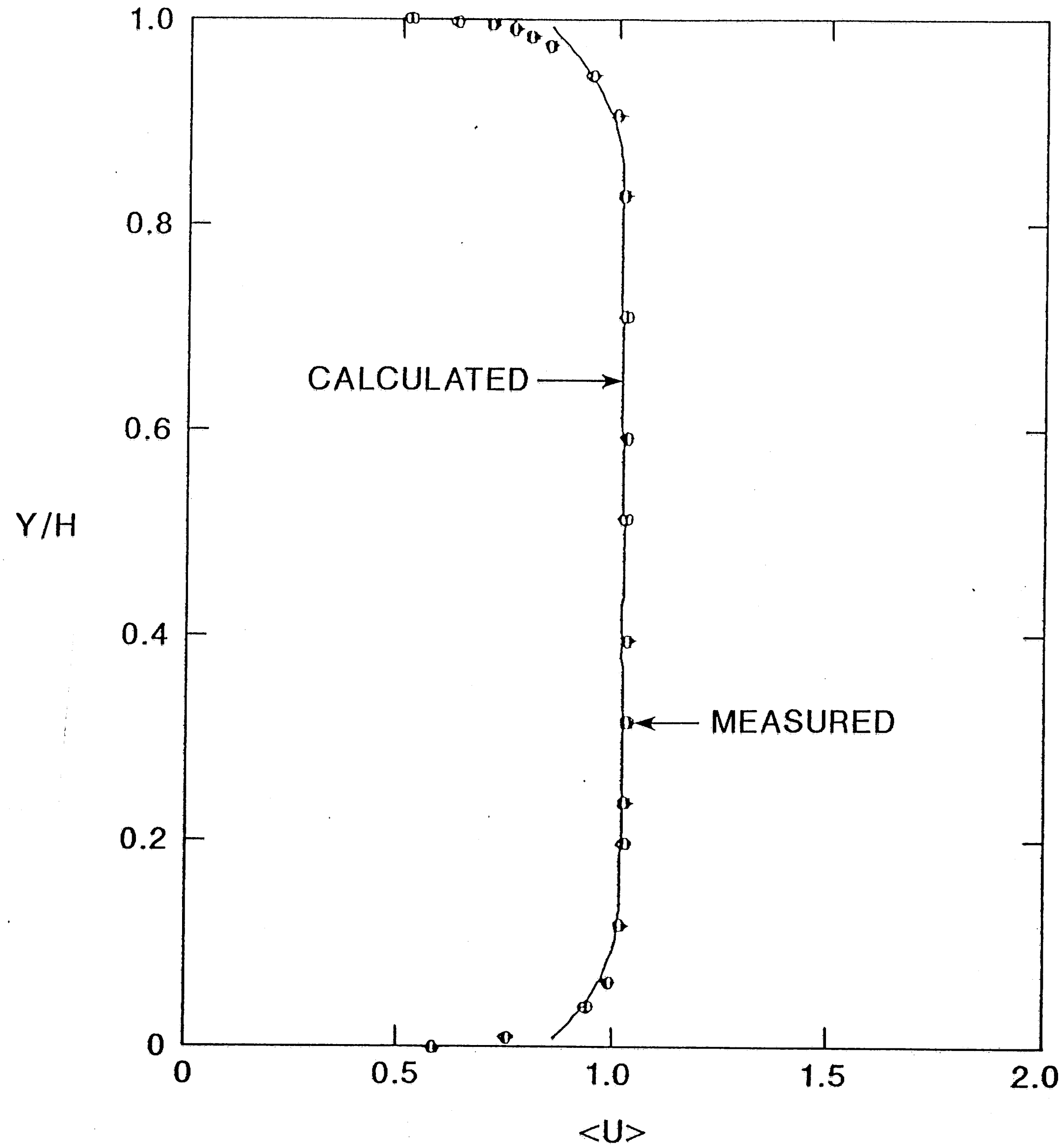

Fig. 17 Comparison of calculated and measured velocity profile at L3, without honeycomb, Re = 3.2×10^6.

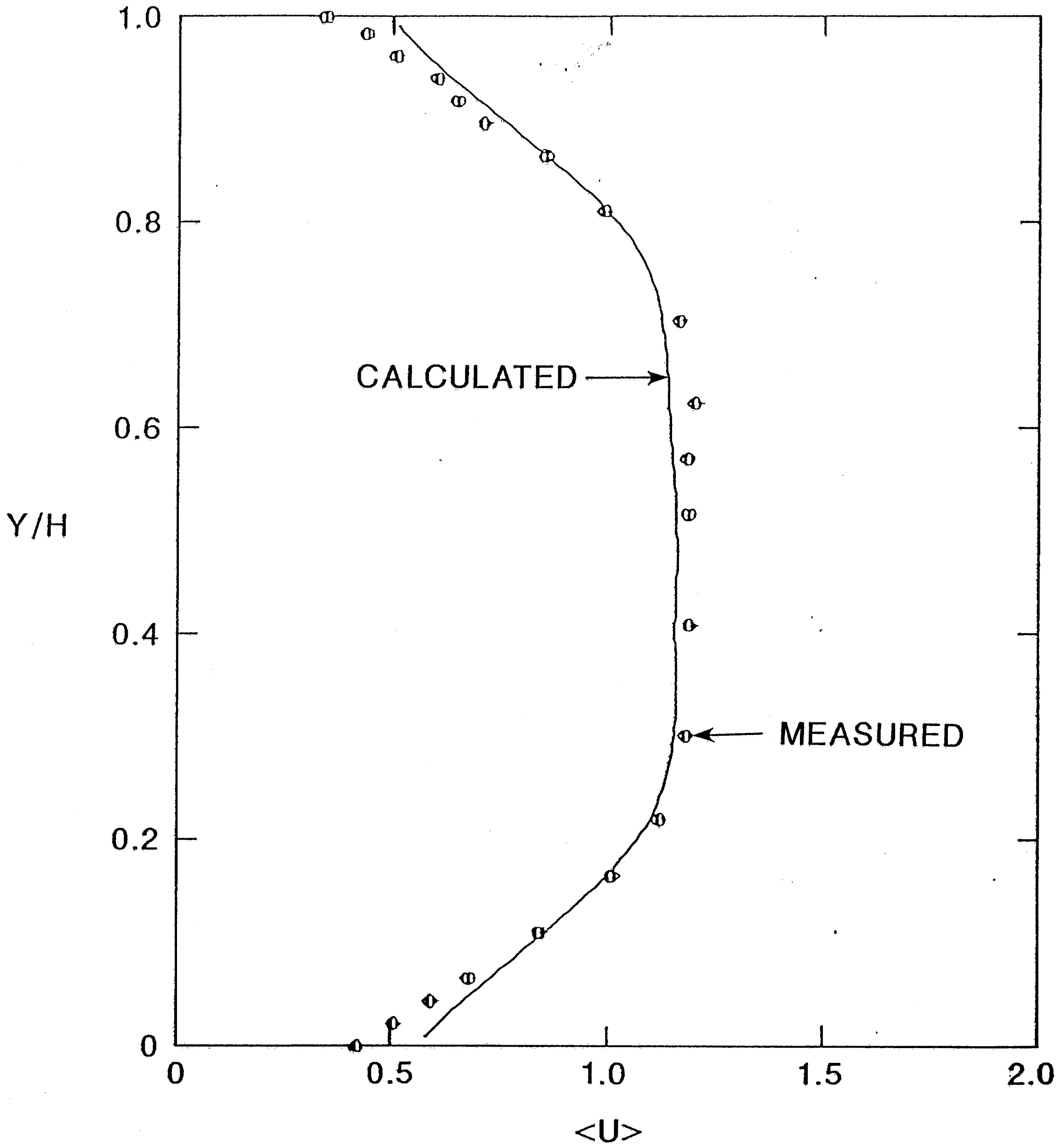

Fig. 18 Comparison of calculated and measured velocity profile at L4, without honeycomb, Re = 3.2×10^6.

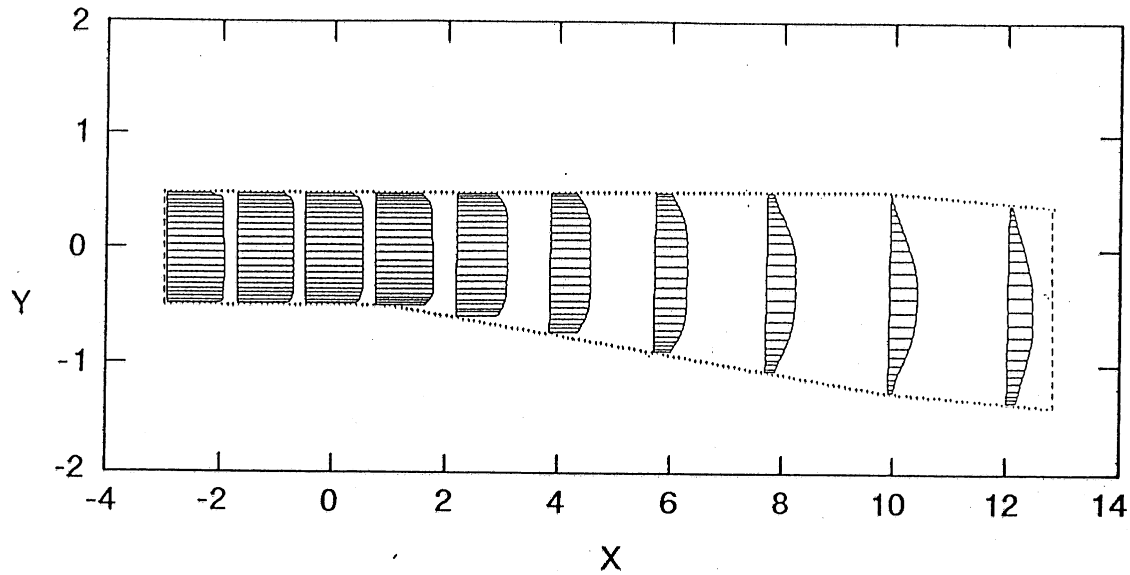

Fig. 19 Velocity profiles at various cross sections as calculated by the modified 2–D model, Re = 3.2×10^6, without honeycomb.

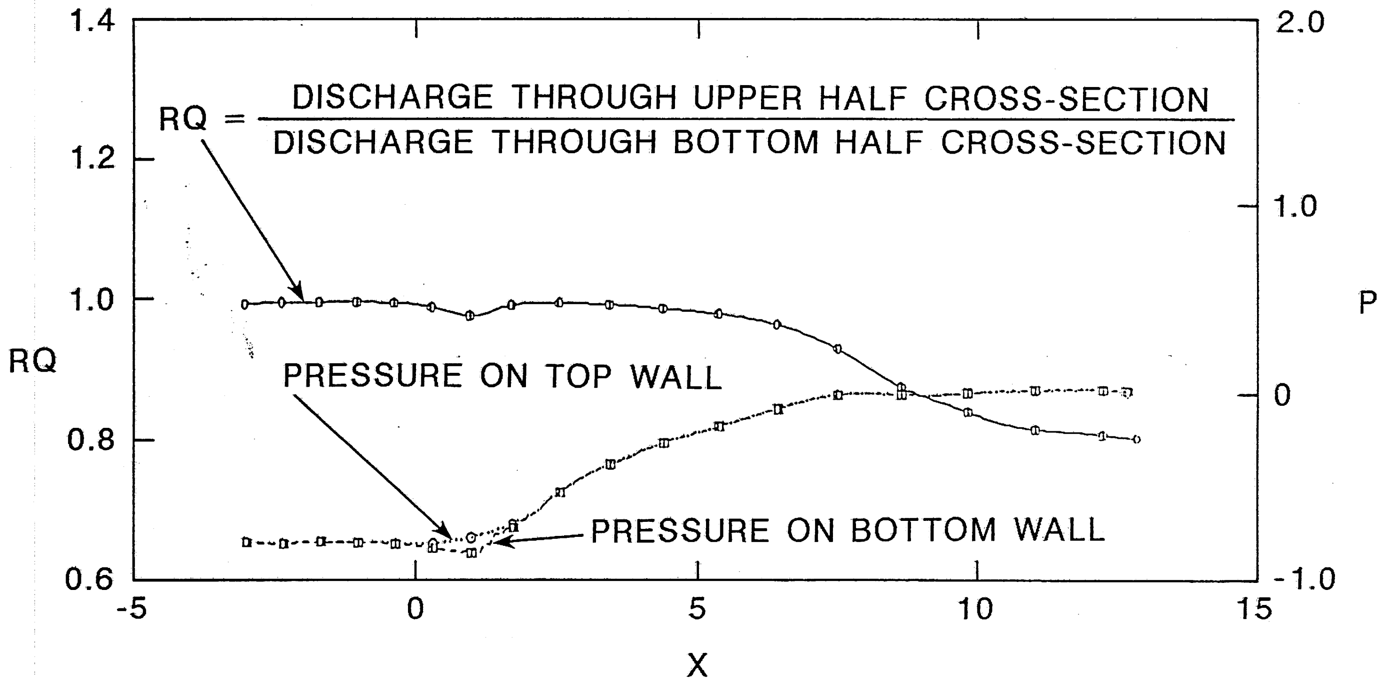

Fig. 20 Calculated discharge ratio and the wall pressure distribution, Re = $3.2\text{x}10^6$, without honeycomb.

Case 2. LDV measurement and honeycomb ($Re = 3.2x10^6$)

Figure 21 shows the calculated and the measured velocity distributions at L3. The corresponding values at L4 are shown in Figure 22. As shown in Fig. 22, the measured velocity distribution contains an S-shaped abnormal velocity distribution near the upper wall which is not predicted by this particular mathematical model. More detailed analysis and discussion of this deviation from normal velocity profile will be given in a later section.

Computed velocity profiles at various cross sections are plotted in Fig. 23. This plot gives a hint of small separation bubbles existing on the upper wall near the diffuser exit. A more detailed velocity vector field clearly indicates that there is a slightly larger separation bubble in this case than in Case 1.

Case 3. Pitot tube measurement with MOD1 honeycomb ($Re = 7.5\times10^5 \sim 1.7x10^6$)

The original honeycomb, referred to a MODO, produced a very thick boundary layer on the top wall and a poor velocity distribution in the test section. In an attempt to speed up the flow near the top wall, the honeycomb was cut and some material near the top wall was removed. This modified honeycomb is referred to as MOD1. Pitot tubes were used to measure the time-averaged velocity distributions at a number of locations indicated in Fig. 1. Circles shown in Fig. 24 represent velocities measured at the test section entrance (P5) when the Reynolds number was equal to 7.5×10^5. This velocity distribution, interpreted as the continuous curve, as shown in Fig. 24, was used as the upstream boundary condition for mathematical modeling. The calculated velocity distribution at P6 is compared with the measured values for $Re = 7.5\times10^5$ in Fig. 25.

Circular symbols shown in Fig. 26 represent the velocity data measured at P7 when the Reynolds number was equal to 1.7×10^6. A direct comparison of the data with computational results is not possible because the Reynolds number was not held constant while data were taken at different locations. The solid line shown in Fig. 26 represents the calculated velocity profile at P7 for $Re = 1.7\times10^6$ assuming that the inflow velocity profile is the same as that of Fig. 24. This inflow velocity profile may be somewhat different from the actual velocity profile which produced the data at P7. This is rather unfortunate because the most important factor affecting the diffuser flow is the inflow velocity distribution. The calculated velocity distribution indicates flow separation on the upper wall near P7. The pitot tube data showing a zone of nearly constant speed is a little difficult to understand. Since the pitot tube measurement is based on pressure sensing, data may actually indicate flow separation rather than constant speed. Velocity profiles calculated for several cross sections at the same condition are shown in Fig. 27. This plot clearly shows that the separated flow occurring on the upper wall extends to the downstream end of the model.

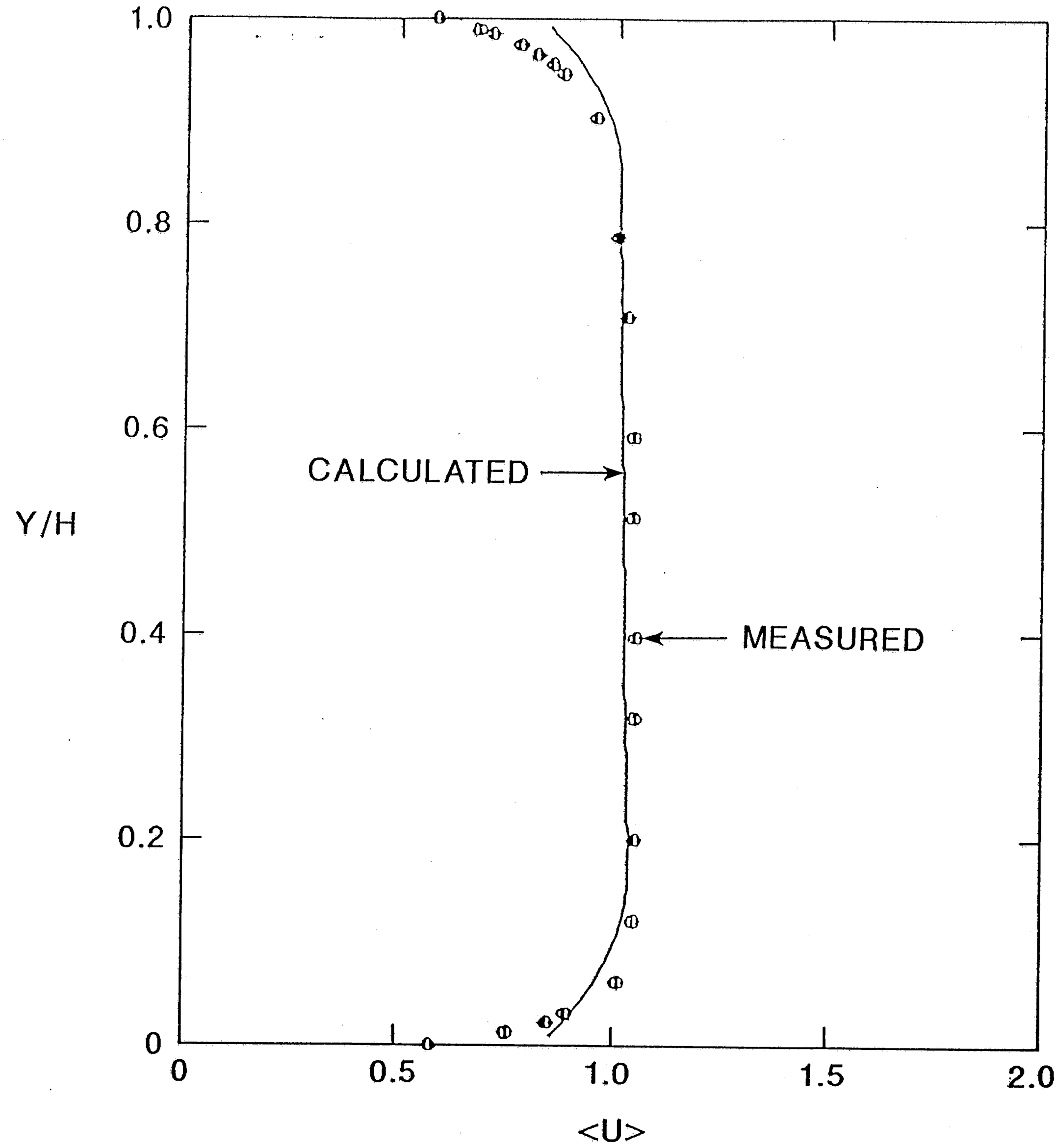

Fig. 21 Comparison of calculated and measured velocity profile at L3, Re = 3.2×10^6, with honeycomb.

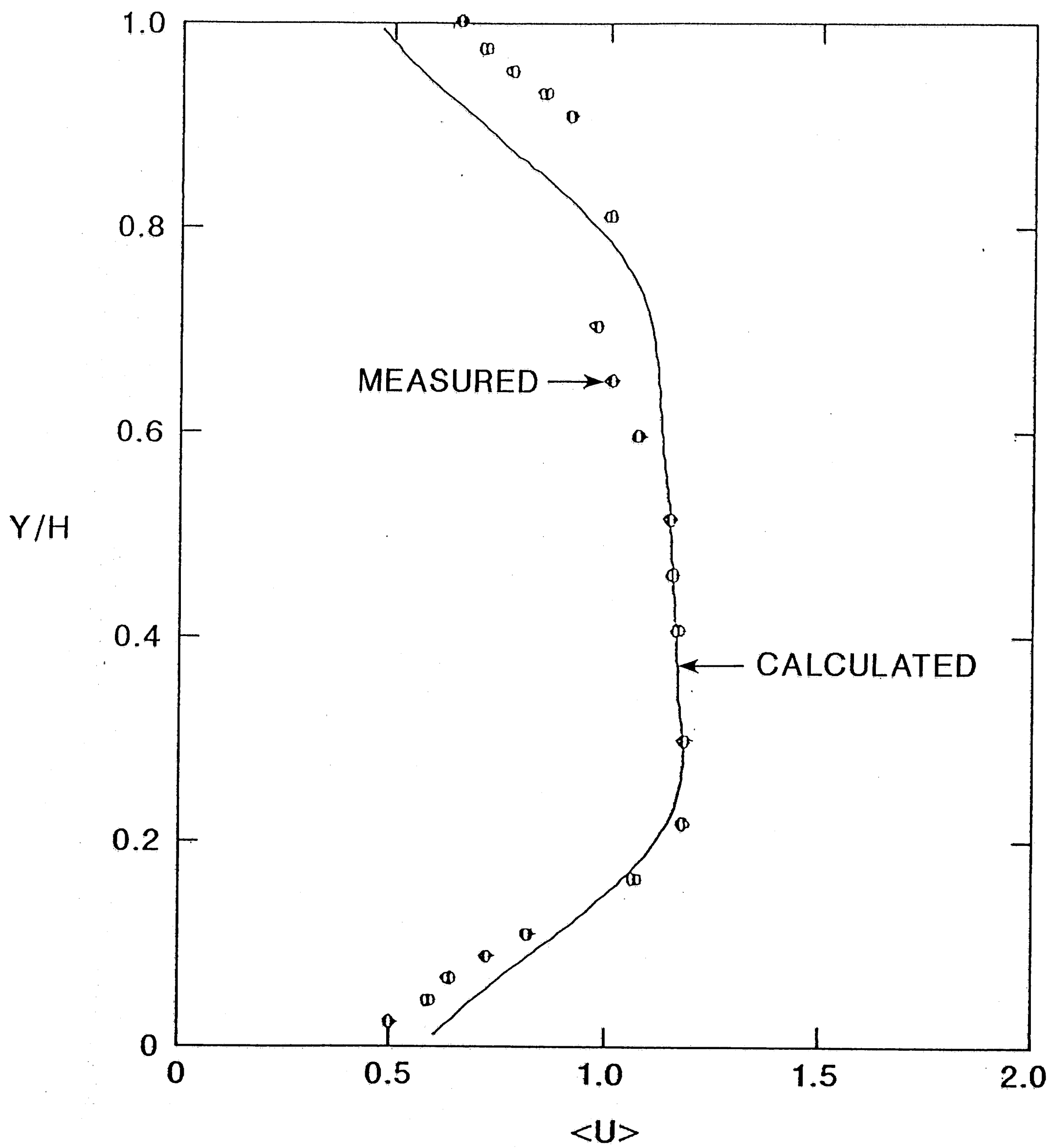

Fig. 22 Comparison of calculated and measured velocity profile at L4, Re = 3.2×10^6, with honeycomb.

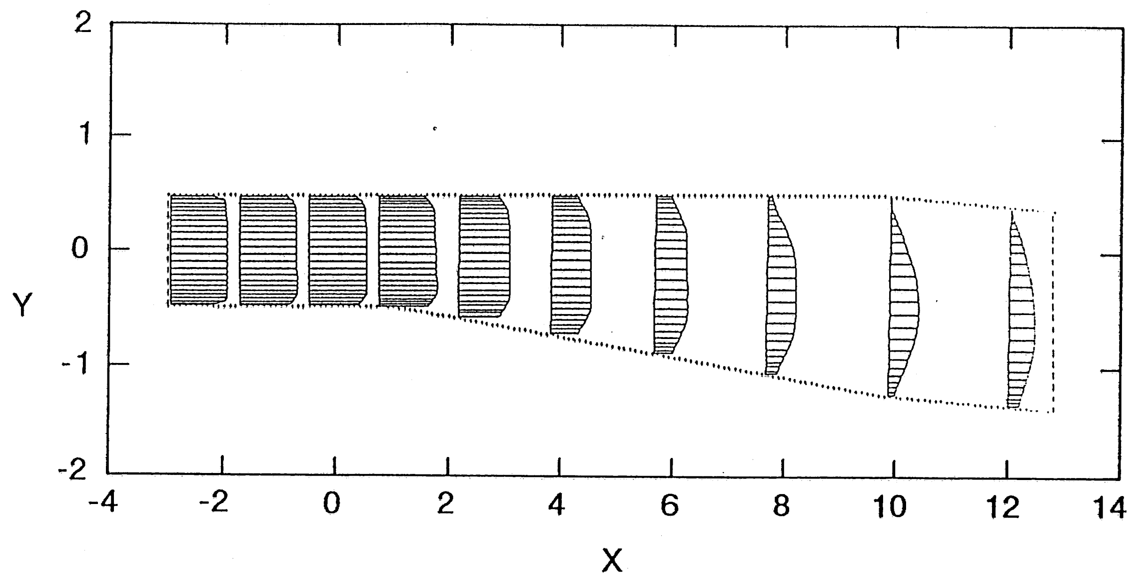

Fig. 23 Velocity profiles at various cross sections as calculated by the modified 2–D model, Re = $3.2\text{x}10^6$, with honeycomb.

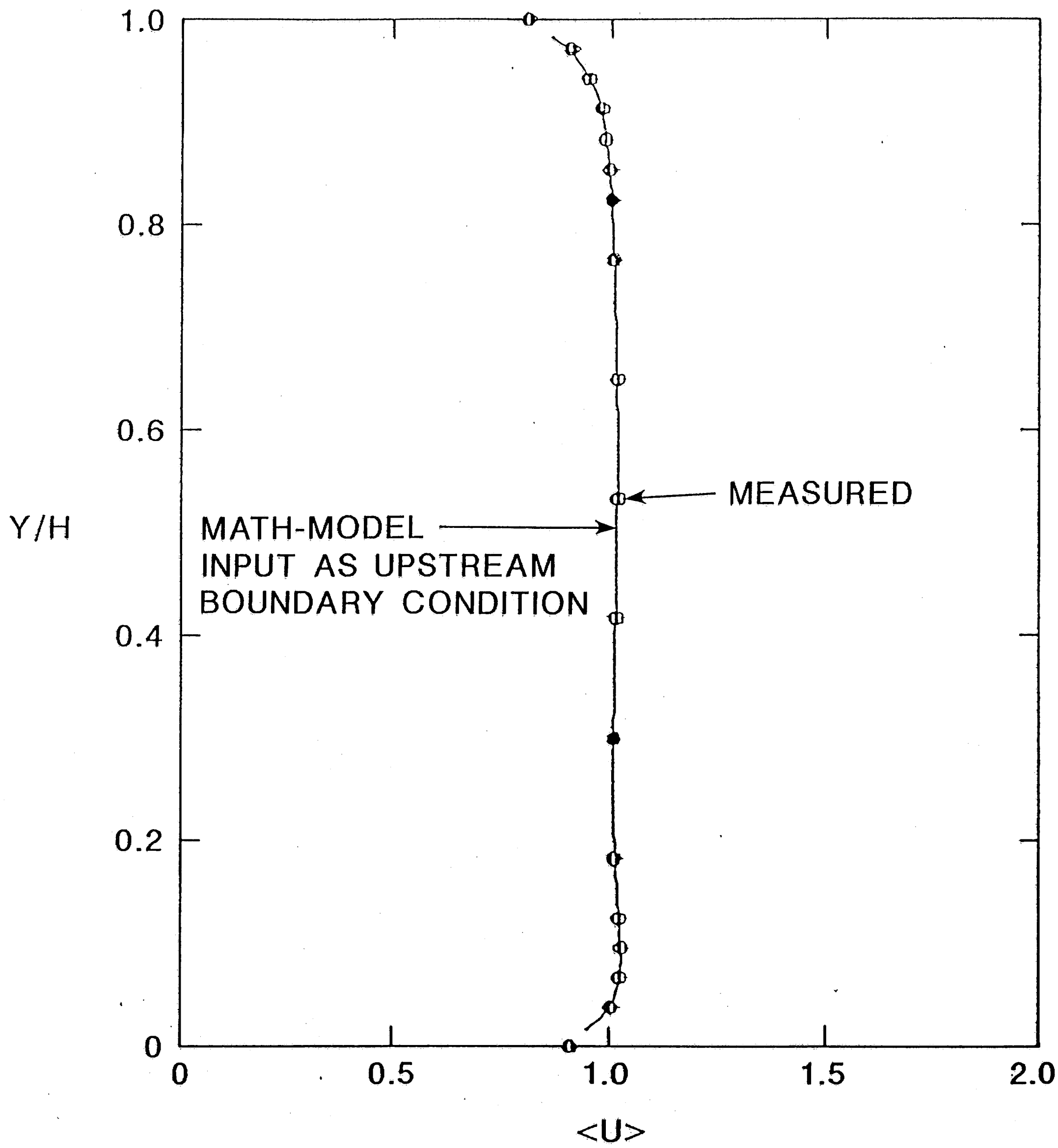

Fig. 24 Measured velocity profile at P5 and the profile used as the upstream end boundary condition, with MOD1 honeycomb, Re = 7.5×10^5.

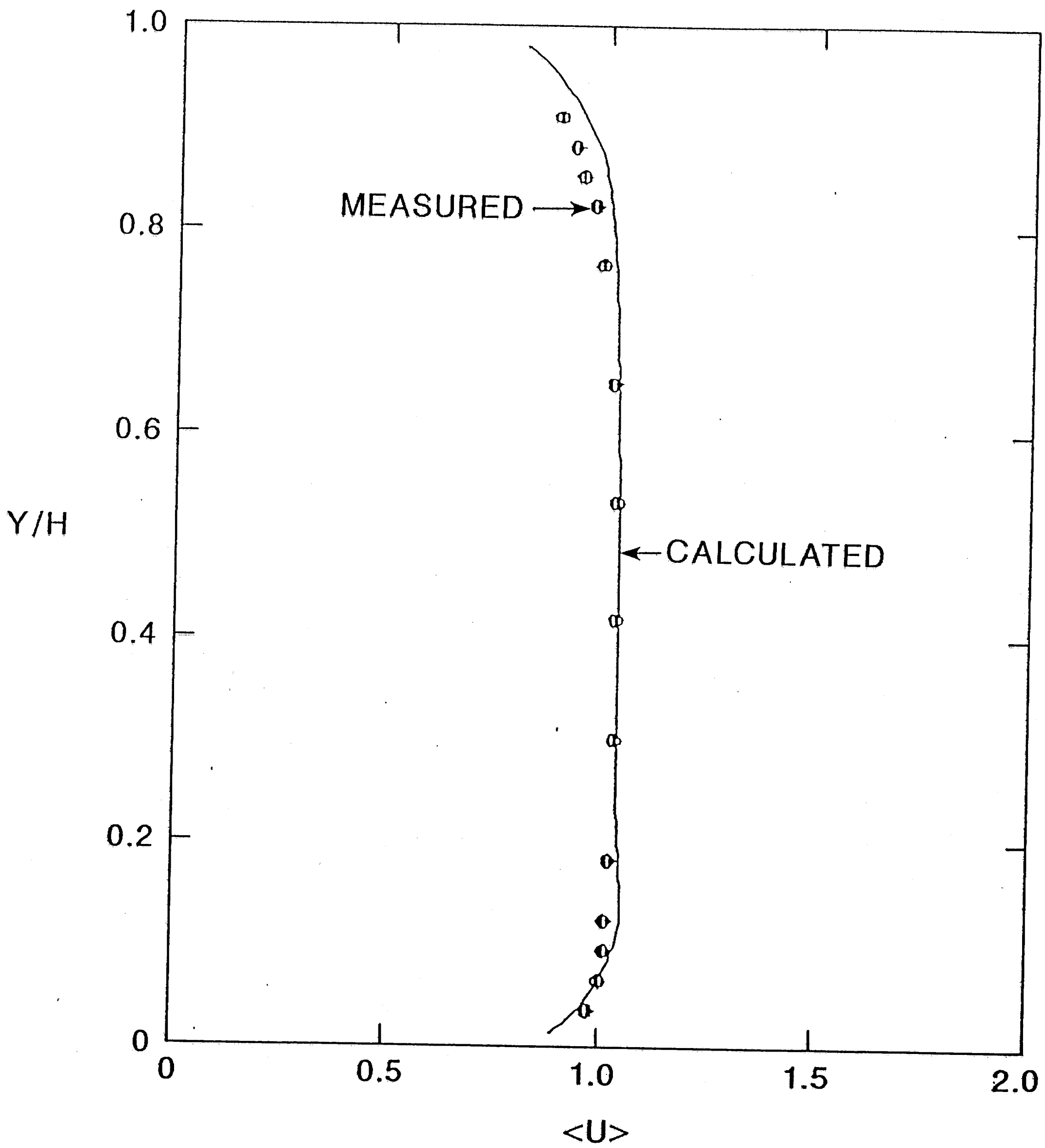

Fig. 25 Comparison of calculated and measured velocity profile at P6, with velocity profile in Fig. 11 as input, Re = 7.5×10^5.

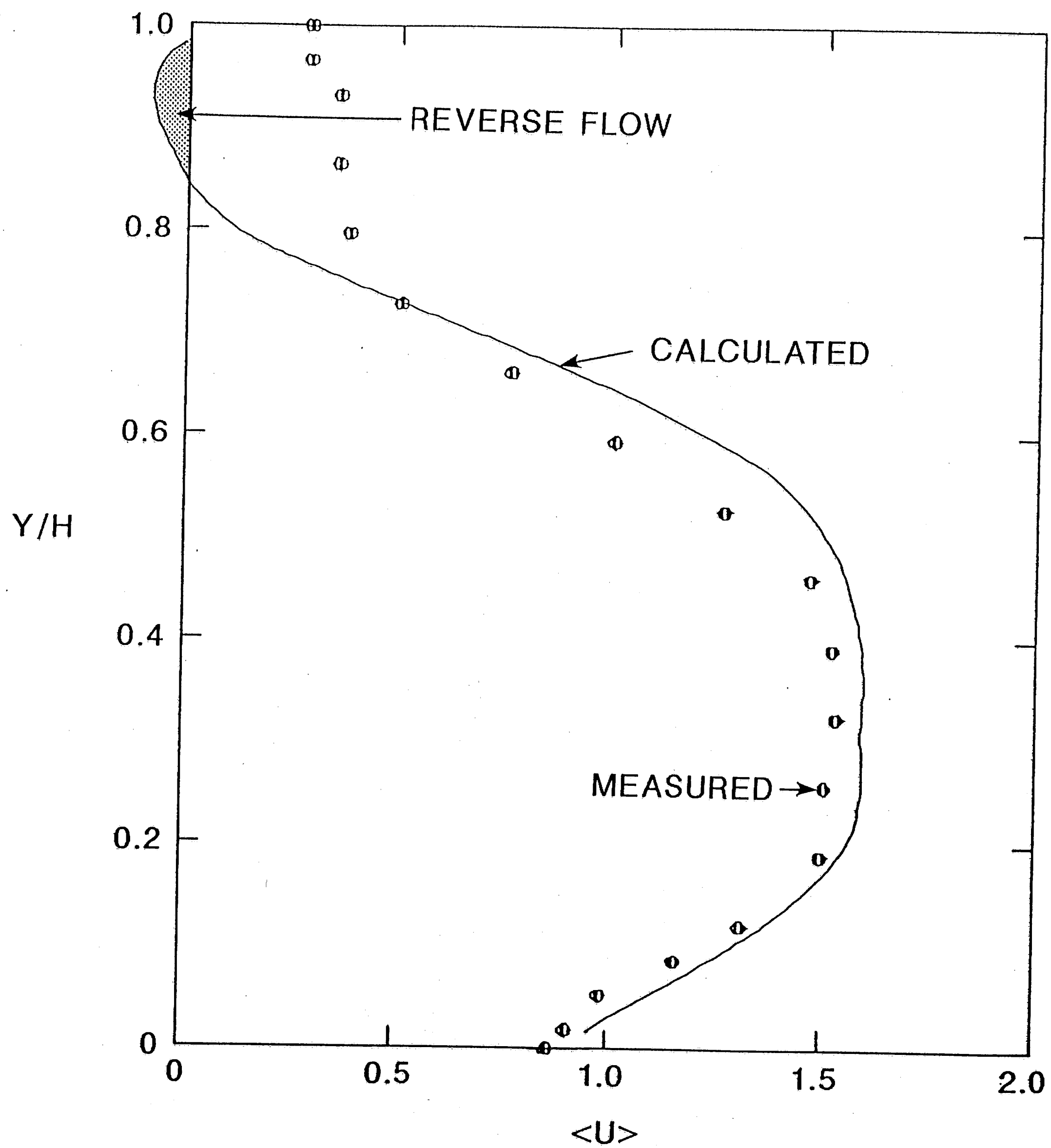

Fig. 26 Comparison of velocity distribution at P7, data taken at Re = 1.7 x10^6, calculation made for Re = 1.7x10^6 using inflow profile measured at Re = 7.5x10^5.

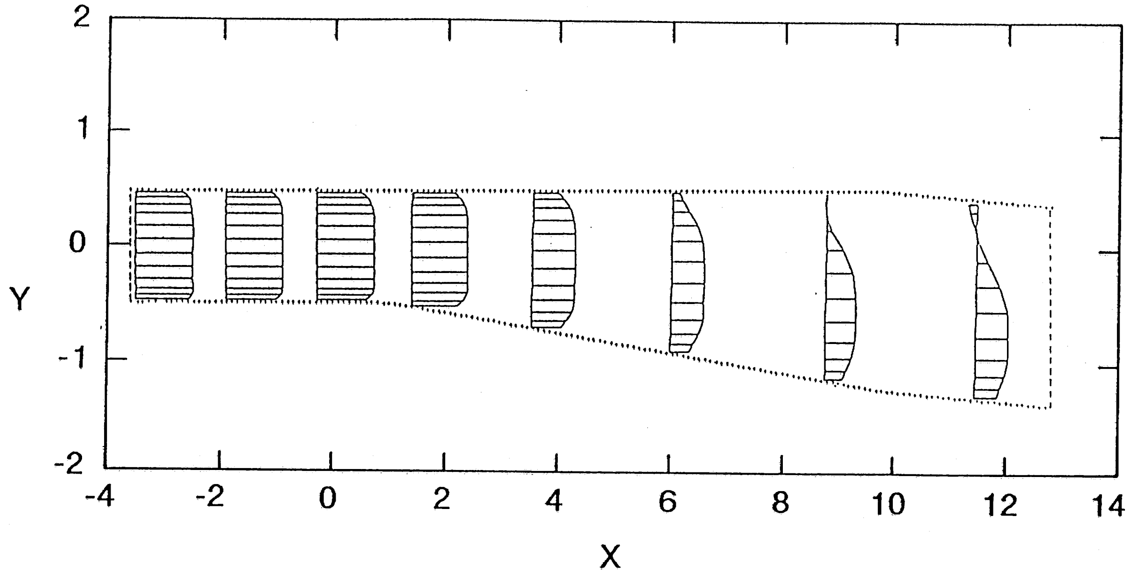

Fig. 27 Velocity profiles calculated for Re = 1.7×10^6 using inflow velocity profile measured at Re = 7.5×10^5.

The calculated pressure distributions along the two walls and the discharge ratio are shown in Fig. 28. As compared with the wall pressure distribution, the discharge ratio is a much more sensitive parameter indicating flow separation and changing velocity distribution. RQ drops to 0.25 at the diffuser end indicating that three times more flow goes through the bottom half of the diffuser than the top half.

Case 4. Reynolds number effects

Calculated velocity distribution for the prototype Reynold number ($Re = 4.5 \times 10^7$) while using the measured velocity profile at P5 for MOD1 at $Re = 7.5 \times 10^5$ as the upstream boundary condition is shown in Fig. 29. When this figure is compared with Fig. 27, it is possible to detect that increasing Reynolds number, without changing the inflow velocity profile, can slightly improve the flow uniformity.

Calculated velocity distribution for $Re = 4.5 \times 10^7$ while using the measured velocity profile at L2 without honeycomb at $Re = 3.2 \times 10^6$ as the upstream boundary condition is shown in Fig. 30. There is no flow separation according to this figure.

Calculated velocity distribution for $Re = 4.5 \times 10^7$, using the measured velocity profile at L2 with MODO honeycomb at $Re = 3.2 \times 10^6$ as the upstream boundary condition, is shown in Fig. 31. Again, there is no flow separation.

Case 5. Simulation of Local Velocity Perturbation

The mechanism of s–shape velocity perturbation measured at L3 as described under Case 2 and shown in Fig. 22 is analyzed herein. Because the velocity profile was measured over a fairly long period of time it is logical to assume that the perturbation is permanent rather than transient. Indeed, numerical experiments indicate that the velocity perturbation of the kind shown in Fig. 22 cannot be produced by periodical introduction of eddies at a point on the upstream end boundary. On the other hand, the required velocity profile was successfully reproduced by introducing a small amount of correction to the inflow velocity profile as described below.

Let $u_o(y/H)$, $u_1(y/H)$, and $u'(h/H)$ be, respectively, the original velocity profile at the entrance, the modified velocity profile at the entrance, and the amount of modification required. That is

$$u_1(y/H) = u_o(y/H) + u'(y/H) \tag{18}$$

where H is the distance between two walls and y is measured from the bottom wall. By numerical experiments, the following modification was found to give good results:

$$\text{for } y/H \geq 0.5,\ u' = -\ 0.03 \text{ Sin } 4\pi\ (y/H - 0.5) \tag{19}$$

$$\text{for } y/H < 0.5,\ u' = 0 \tag{20}$$

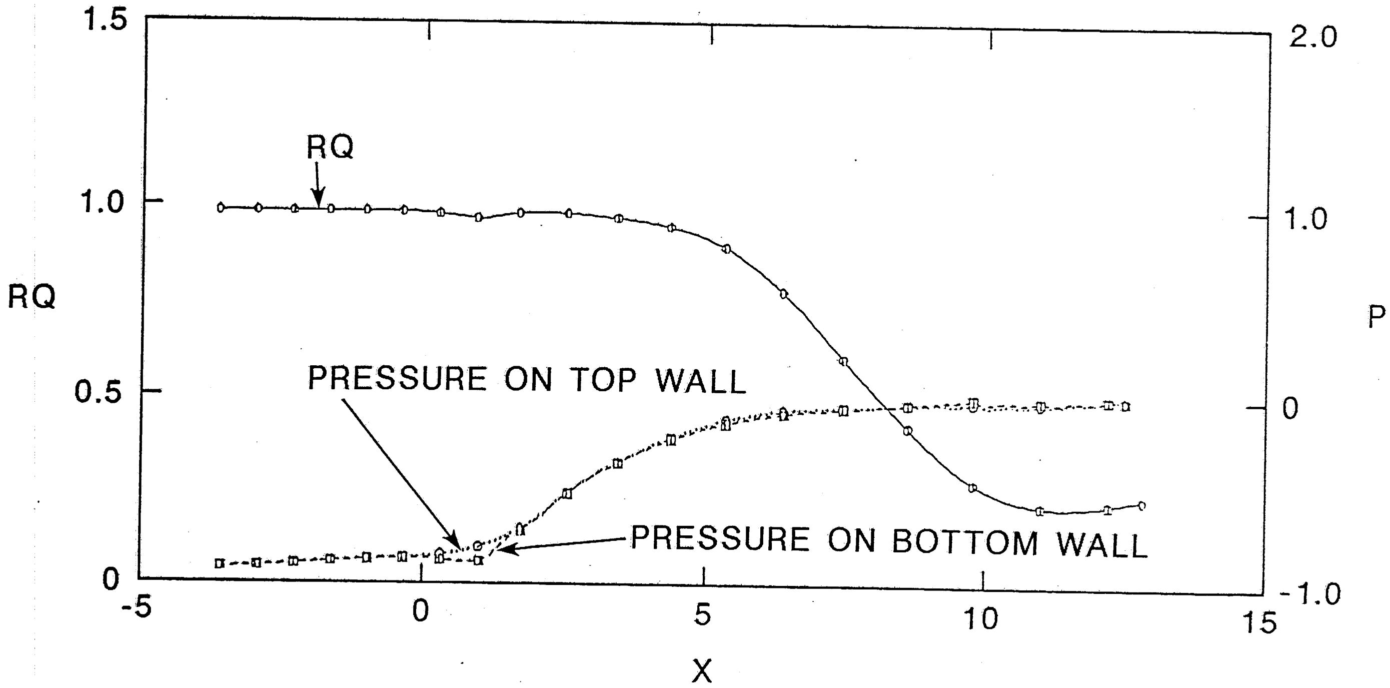

Fig. 28 Calculated pressure distribution on the walls and the discharge ratio, Re = 1.7×10^6.

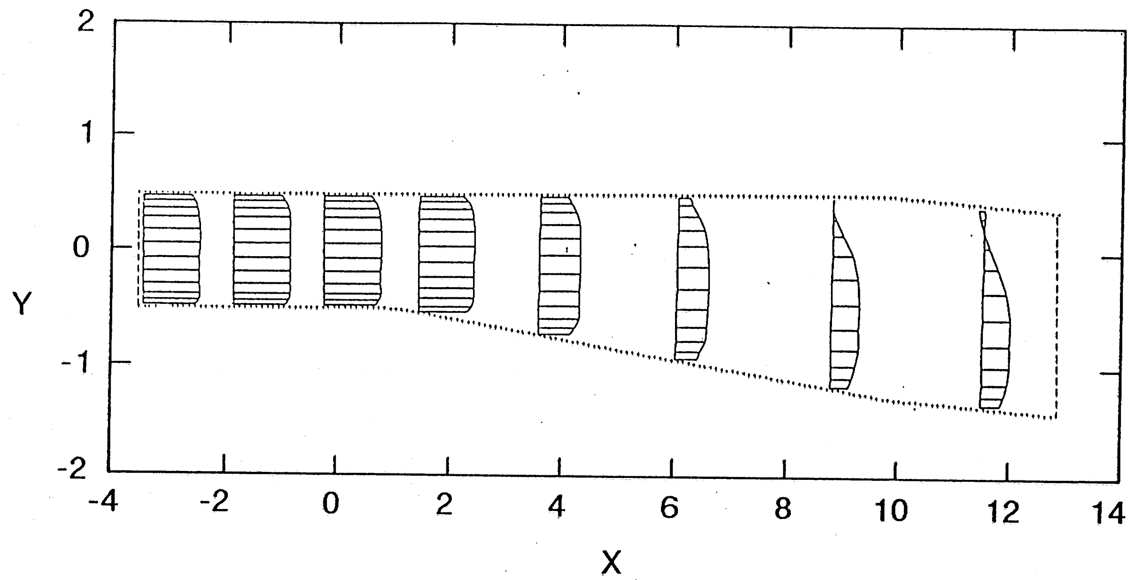

Fig. 29 Calculated velocity distribution for Re = $4.5x10^7$, using data for MOD1 at Re = $7.5x10^5$ as upstream boundary condition.

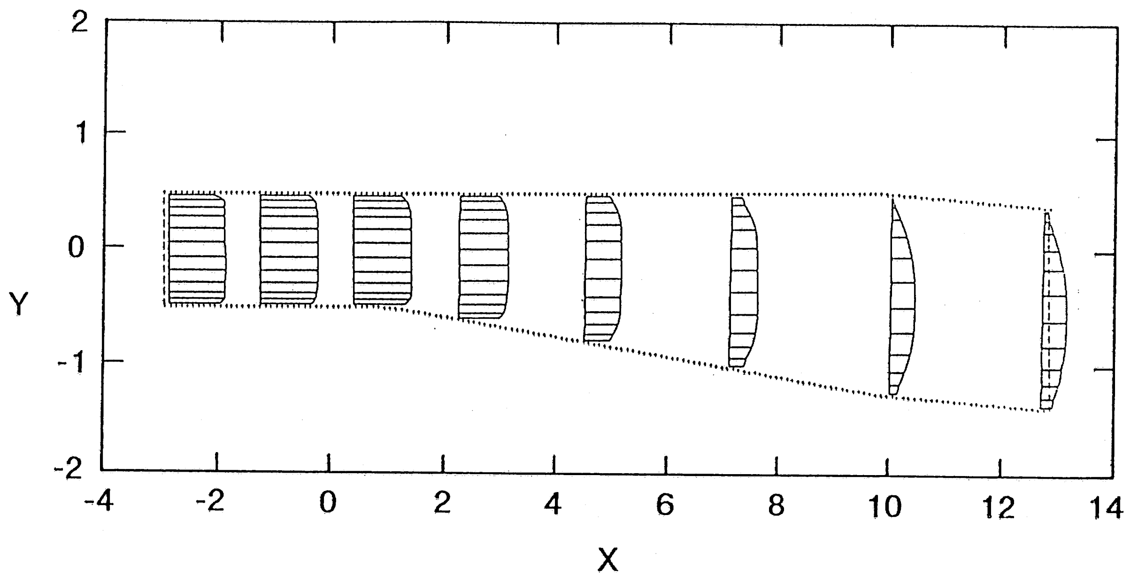

Fig. 30 Calculated velocity distribution for Re = 4.5×10^7 using data for Re = 3.2×10^6 without honeycomb as upstream boundary condition.

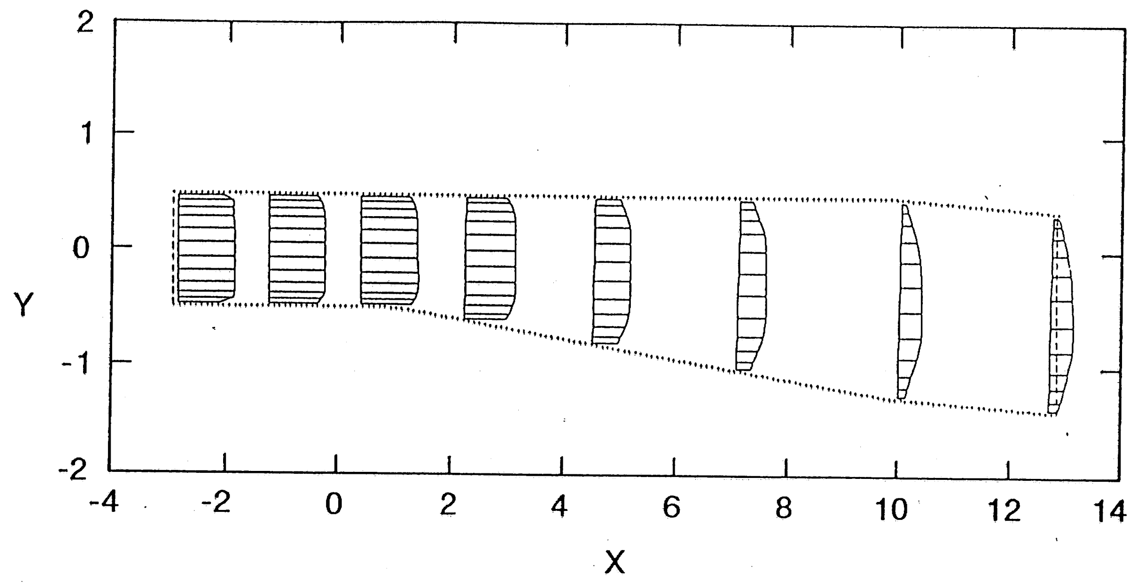

Fig. 31 Calculated velocity distribution for Re = 4.5×10^7 using data for Re = 3.2×10^6 with MOD0 type honeycomb.

The imposed perturbation is a fixed sinusoidal variation over the upper half of the cross section having an amplitude equal to 3 percent of the mean velocity.

The calculated velocity distributions at L3 and L4 are compared with the measured values in Figs. 32 and 33, respectively. Very significant improvement has been achieved for Station L4 but the effect of the modification on the velocity distribution at L3 is not significant. As it has already been noted that the velocity nonuniformity at the inlet tends to be magnified by a diffuser.

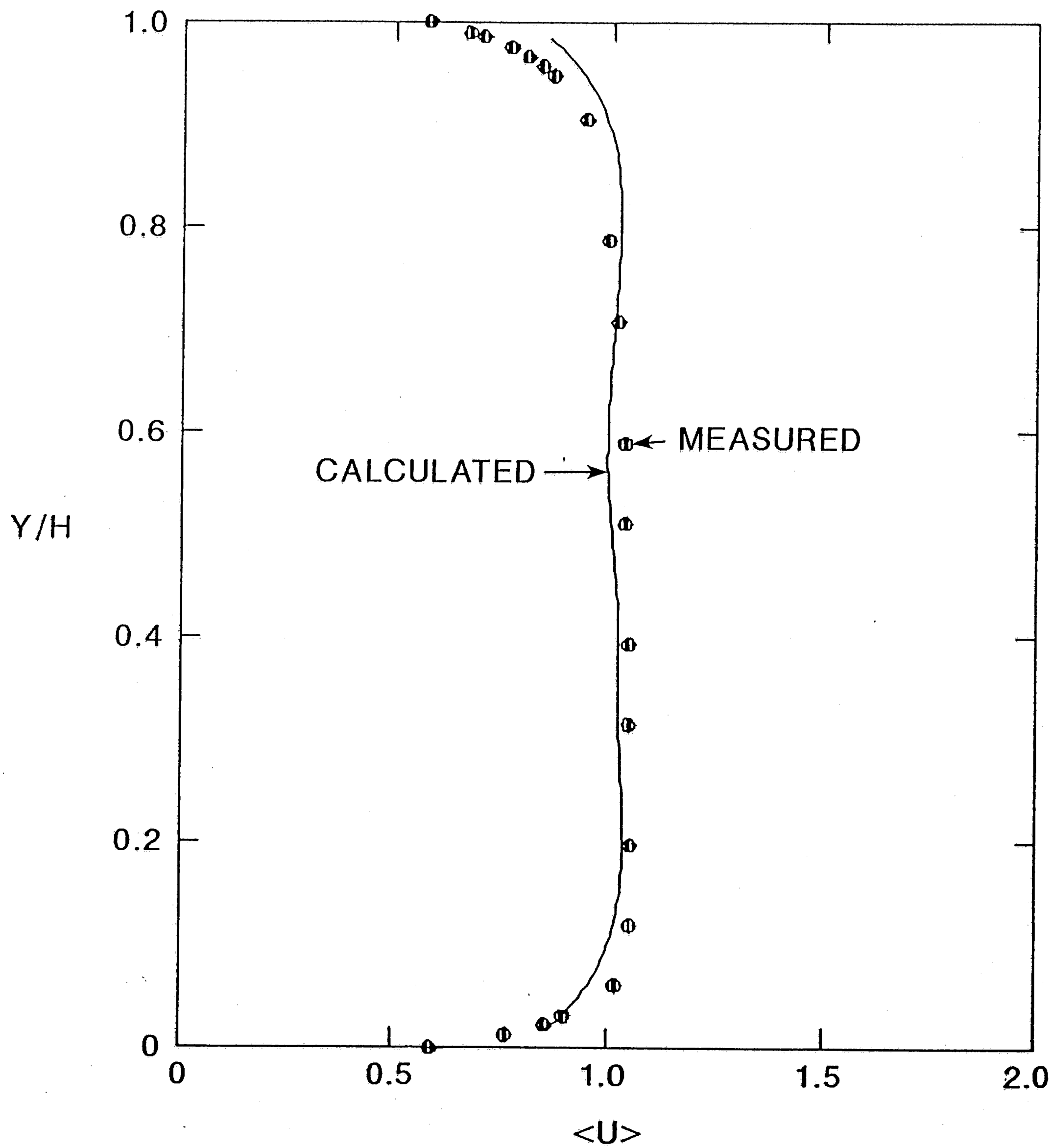

Fig. 32 Comparison of calculated and measured velocity profile at L3 with modified inflow velocity profile, Re = $3.2x10^6$, with honeycomb.

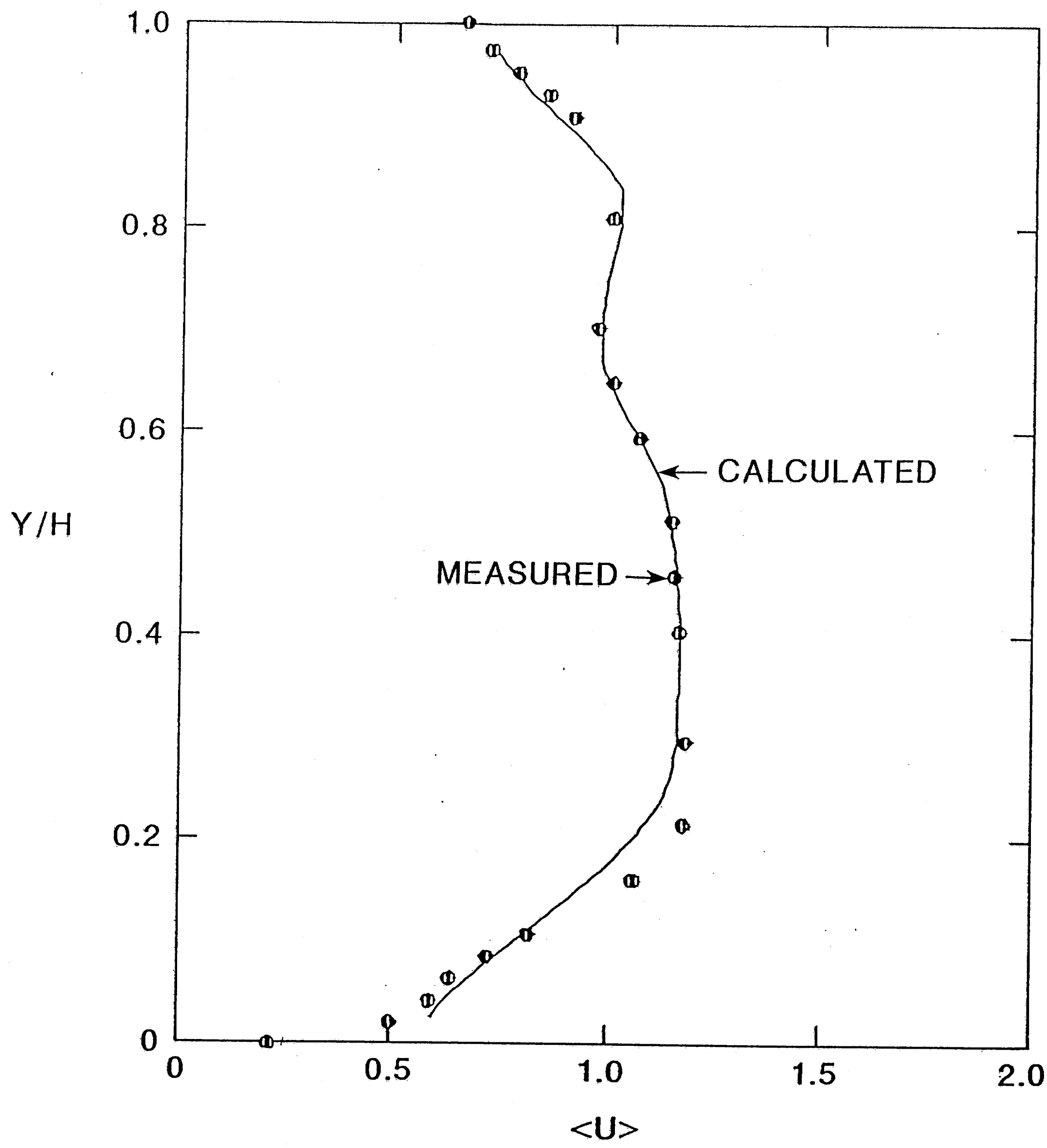

Fig. 33 Comparison of calculated and measured velocity profile at L4 with modified inflow velocity profile, Re = $3.2x10^6$, with honeycomb.

IV. CONCLUSIONS

1. A three–dimensional diffuser intensifies the vorticity due to stretching. For this reason, transverse velocity field sat the contraction entrance may be reorganized into a stronger secondary current at the contraction exit. In other words, the guide vanes and honeycomb located upstream of the contraction should be carefully installed to minimize the transverse velocity components.

2. The existence of thick boundary layer on the upper wall in the test section of the 1:14 scale model is the reflection of poor inflow quality.

3. Two possible explanations are offered for the poor velocity distribution existed at the contraction entrance of the 1:14 scale model. The first possibility is the disturbance of the velocity distribution by the honeycomb. The second possibility is the positive feed–back effect involving flow separation in the diffuser. When the flow separates from the upper wall and diverts the flow toward the lower wall of the diffuser, the resulting unbalanced flow may be carried around the circuit to the contraction entrance resulting in a deficit near the upper wall at the entrance.

4. The diffuser is near the critical condition in the Reynolds number range of the 1:14 scale model flows. Mathematical modeling indicates that the flow separation had occurred in the 1:14 scale model when tested with the honeycomb. This was not detected by the measurements because, for most cases, the separation occurred downstream of stations where measurements were taken. A strong evidence of flow separation is provided by the data shown in Fig. 26.

5. The most critical factor for diffuser performance is the quality of the inflow velocity profile, especially the boundary layer thickness. A small change in the boundary layer thickness is greatly magnified by the diffuser, due to the adverse pressure gradient.

6. Because the existence of adverse pressure gradient and boundary layer are the two primary factors regarding flow separation, the asymmetric diffuser does not act like a symmetrical diffuser having twice the total diffusion angle. It is the total diffusion including the horizontal diffusion and the vertical diffusion that is the major determining factor.

7. The reason for the s–shaped deviation from normal velocity distribution at station L4 and, to a less extent, at station L3, is very likely due to the existence of a shear layer at about 0.25 H below the upper wall at the entrance. The intensity of the shear layer required at the test section entrance is only 3 percent of the average flow velocity.

8. By increasing the Reynold number, the flow quality can be improved for two reasons: (a) the boundary layer at a diffuser entrance is made thinner, and (b) larger Reynold numbers promote momentum exchange in the diffuser.

9. It appears that the quality of the velocity profile in the prototype LCC, at Re near 4.5×10^7, will be much better than that of the 1:14 model.

10. No significant changes are necessary for the hydrodynamic forces previously estimated.

REFERENCES

1. Model Test Data, Pump Velocity Surveys, Voith Hydro, Inc., 1987.

2. Facsimile Transmittal from DTRC, LCC project office, March 7, 1988, from Bob Etter to Joseph Wetzel.

3. Song, C.C.S., J. M. Wetzel, J. M. Killen, and R.E.A. Arndt, "Physical and Mathematical Modeling of the HYKAT," St. Anthony Falls Hydraulic Laboratory, University of Minnesota, Project Report No. 282, Dec. 1988.

4. Song, C.C.S and M. Yuan, "A weakly compressible flow model and rapid convergence methods," *Jour. of Fluids Engineering*, ASME, Vol. 110, No. 4, Dec. 1988, pp. 441–445.

5. MacCormack, R. W., "The effect of viscosity in hypervelocity impact cratering, AIAA Paper No. 69–354, May 1969.

6. Schumann, U., G. Grotzbach and L. Kleiser, "Direct numerical simulation of turbulence," *Prediction Methods of Turbulent Flows*, edited by W. Kollmann, Hemisphere Publishing Corp., New York, 1980, pp. 124–158.

7. Smagorinsky, J., "General Circulation Experiments with Primitive Equations," *Monthy Weath. Rev.*, Vol. 91, No. 3, 1963.

8. Ferziger, J. H., "Simulation of incompressible turbulence flows," *Jour. Comp. Phys.*, Vol. 69, 1987, pp. 1–48.

9. Roggallo, R. S. and P. Moin, "Numerical simulation of turbulent flow," *Ann. Rev. of Fluid Mech.*, Vol. 16, 1984, pp. 99–137.

10. Letter from Charles C. S. Song to Bob Etter, September 29, 1987.